Università degli studi di Padova

Dipartimento di Fisica e Astronomia "Galileo Galilei"

Master Degree in Physics

Final Dissertation

Quantum many-body effects in a π-flux Hubbard model

Supervisor
Prof. Marco Di Liberto

Co-supervisor
Dr. Lorenzo Maffi

Candidate
Maria Sharon Di Spena

Academic Year
2024-2025

Abstract

Frustration and synthetic magnetic fluxes have emerged as pivotal tools in the exploration of novel many-body quantum phases in ultracold atomic systems. A particularly non-trivial framework involves the introduction of a π-flux, which gives rise to topologically non-trivial band structures and enables spontaneous breaking of time-reversal symmetry, a key feature in the emergence of chiral phases. Building on recent two-dimensional studies, we investigate the many-body physics of a three-dimensional generalization of the π-flux Bose-Hubbard model, involving bosonic particles on strongly dimerized cubic plaquettes. We construct a low-energy effective model that we benchmark via exact diagonalization of the full model, revealing filling-dependent degeneracies and regularities in the energy spectrum. These regularities hint at the presence of underlying hidden symmetries in the model, that we attempt to classify by developing a group theory analysis and recasting the effective Hamiltonian in terms of an $SU(4)$ algebraic description. In the weakly interacting regime, a Gross–Pitaevskii analysis uncovers a 12-fold degenerate manifold of classical ground states characterized by chiral loop current patterns flowing on the edges of the cubic cell. Our results establish the 3D π-flux cube as a minimal model for investigating many-body physics in higher dimensions and novel chiral states relevant for quantum simulation platforms based on ultra-cold atoms in synthetic gauge fields.

Contents

1 Introduction

One of the central goals in modern condensed matter physics is the exploration of exotic quantum phases that go beyond the Landau symmetry-breaking paradigm, where the characterization of different phases and their universal features relies on the definition of a local order parameter. In this direction, the interplay of time-reversal symmetry-breaking and many-body interactions turns up to have a fundamental role in the emergence and stabilization of novel phases of matter. In particular, magnetic frustration combined with strong interactions is shown to give rise to intriguing macroscopic quantum phenomena, driving the formation of strongly correlated phases characterized by non-local properties such as ground state degeneracy, quantized responses, and robust boundary excitations and defined by a new type of global order called topological order [1].

A paradigmatic example of such phenomena is the quantum Hall effect (QHE) [2]. First observed in the early 1980s, the QHE demonstrated that a two-dimensional electron gas subjected to a strong perpendicular magnetic field (see Fig. 1.1) and placed at very low temperature can exhibit quantized Hall conductance at integer [3] or fractional values [4] of the fundamental unit e^2/h, and this quantization is insensitive to imperfections or disorder in the samples. Quantum Hall states are characterized by gapped bulk and massless chiral excitations at the edge of the system, with edge modes that are typical signatures of topological states. In particular, in fractional quantum Hall systems, strong magnetic fields and electron-electron interactions give rise to incompressible quantum fluids with fractionally charged excitations [5]. In 1983, Laughlin's seminal paper [5] provided the theoretical ansatz for fractional Hall states, introducing a many-body wavefunction that accounts for the emergence of quasi-particles carrying fractional charge and realizes a topologically ordered phase [6], characterized by non-local quantum correlations and robustness against local perturbation.

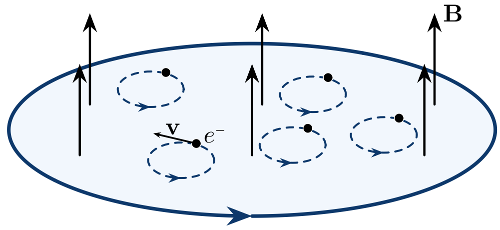

Figure 1.1: Two-dimensional electron system in a strong perpendicular magnetic field $\mathbf{B}$, realizing an integer quantum Hall state in the absence of interactions. The perpendicular magnetic field forces the free (classical) electrons to move on circular orbits at the cyclotron frequency $\omega_c = \frac{eB}{m}$, with tangential velocity indicated by $\mathbf{v}$. While in the bulk electrons move in closed orbits, at the edges of the sample incomplete cyclotron orbits (skipping orbits) propagate unidirectionally under the Lorentz force, carrying a chiral current flowing along the boundary. In the quantum regime the bulk is insulating, while the edge is gapless. The system displays a quantized Hall response.

These developments established the fractional quantum Hall effect (FQHE) as a paradigmatic example of a topologically ordered phase of matter, one that cannot be described within the Ginzburg–Landau paradigm in terms of a local order parameter, featuring global order and protected gapless edge modes in the form of chiral currents flowing along the boundary.

At the basis of the quantum Hall effect lies the structure of Landau levels, schematically depicted in Fig. 1.2: the discrete and macroscopically degenerate single-particle energy levels of a two-dimensional system of charged particles immersed in a perpendicular magnetic field. Within each Landau level, the energy is independent of momentum, effectively producing a perfectly flat band in which kinetic dispersion is quenched. In the integer case, the non-trivial topology of Landau levels is encoded in the non-zero first Chern number [7], a topological invariant associated to completely filled Landau levels and defining the exact integer quantization of the Hall conductivity. In the fractional case, the quantization of the Hall conductivity arises from the emergence of strongly correlated many-body states by partially filling Landau levels. In this regime, electron–electron interactions play a crucial role, giving rise to topological order beyond the single-particle band picture of the integer case. The absence of kinetic dispersion leads to a macroscopic degeneracy that enhances the role of Coulomb interactions, which are no longer screened by kinetic effects and become the primary mechanism governing the many-body ground state. These interactions lift the degeneracy given by partially filled Landau levels and drive the emergence of correlated ground states with topological order describing the FQHE. In this sense, Landau levels provide a natural realization of topological flat bands in continuum systems, where interactions can stabilize strongly correlated phases that can be topological.

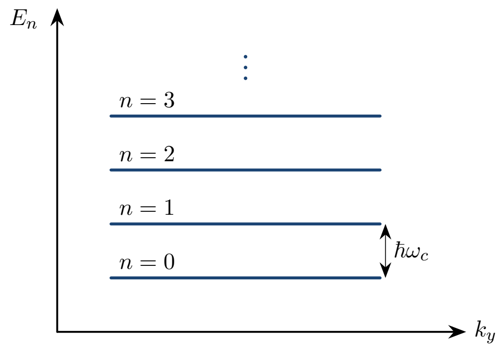

Figure 1.2: Landau levels for a charged particle moving in the (x, y)-plane subjected to a perpendicular magnetic field $\mathbf{B} = \nabla \times \mathbf{A} = B\hat{\mathbf{z}}$. In the Landau gauge $\mathbf{A} = xB\hat{\mathbf{y}}$, the momentum along the y-direction k_y is a good quantum number, labeling the degenerate states within each level. The magnetic field quantizes the energy spectrum into equally spaced energy levels $E_n = \hbar\omega_c \left(n + \frac{1}{2}\right)$, with $n \in \mathbb{N}$. Note that the spacing is given by the cyclotron frequency ω_c, which is proportional to B. The number of filled Landau levels ν determines the quantized Hall conductivity $\sigma_{\mathrm{H}} = \nu \frac{e^2}{2\pi\hbar}$ for the IQHE.

While these phenomena were first studied in solid-state systems, the interest in exploring strongly correlated phases within accessible and tunable settings and their relevance in modern technology [8] has led to recent advances in the field of analog quantum simulators.

In particular, ultracold quantum gases confined in optical lattices have emerged as a powerful platform for this purpose, providing a unique framework for simulating strongly correlated many-body systems and exploring topological phenomena and quantum phase transitions in synthetic quantum matter [9–15]. An optical lattice is a crystal of light created by interfering coherent laser beams propagating in opposite directions. Atoms loaded in such a laser field experience the resulting interference pattern as a periodic potential through the light-induced optical dipole force. Ultracold atoms in an optical lattice thus behave analogously to electrons in a crystalline solid, tunneling between periodic potential wells, yet with a tunneling amplitude which can be controlled by tuning the lattice depth. By interfering more counter-propagating laser beams at various angles, periodic potentials can be created in one, two, or three dimensions and a wide range of lattice geometries can be experimentally realized [9, 10]. This high degree of control over interaction strength, lattice geometry and dimensionality allows for the experimental realization of landmark condensed matter models, such as different types of Hubbard models. These are basic models describing particles tunneling between crystalline lattice sites with on-site attractive or repulsive interaction. Notably, in these models the high level of tunability of the ratio between the hopping coupling J and the on-site interaction U has made it

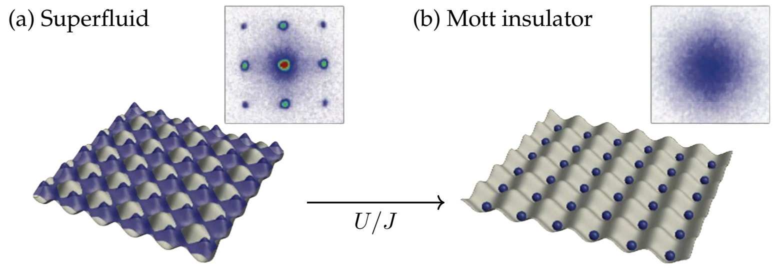

Figure 1.3: Quantum simulation of a bosonic Hubbard model in an optical lattice, taken from Ref. [14]. (a) For weak interactions $U/J \ll 1$, the ground state is a superfluid. Atoms are described by a coherent macroscopic wavefunction (purple wave) delocalized over the whole lattice, as evidenced by the diffraction pattern arising after the atoms are released from the optical potential (inset). (b) By increasing the lattice potential depth, interactions become ever more dominant with respect to the hopping amplitude. In the strongly interacting regime $U/J \gg 1$, the system undergoes a phase transition to a Mott insulator state: the ground state is a lattice gas in which each boson is localized to one lattice site, and phase coherence disappears.

possible to observe the quantum phase transitions between the superfluid and the Mott insulating phase in a three-dimensional lattice system of interacting bosonic atoms with repulsive interactions, as described by the Bose-Hubbard (BH) Hamiltonian [12, 16, 17]. Experimental evidences from Refs. [14, 17] of the BH phase transition are reported in Fig. 1.3, in which the ultracold bosonic gas is shown to undergo a transition between the two distinct ground states.

In addition to the tuning of interactions in lattice models, the flexibility offered by ultracold atom systems allows the engineering of synthetic gauge fields [18, 19] to mimic the effect of strong magnetic fields and spin–orbit coupling on neutral atoms. These synthetic magnetic fields are typically implemented via lattice rotation, Raman coupling, or laser-assisted tunneling [19, 20]. Remarkably, such engineered magnetic fluxes can reach intensities far beyond those achievable in conventional solid-state systems, extending the accessible parameter regimes and thus opening the way for the simulation of quantum Hall systems and topological quantum matter [21, 22].

A step in this direction is the realization of two-dimensional lattice models of non-interacting particles in the presence of a magnetic field: the so-called Hofstadter model [23]. The effect of the magnetic field is encoded in Aharonov-Bohm phase factors in the tunnelling amplitudes, which explicitly break time-reversal symmetry and frustrate particle motion around closed loops. For rational values of the magnetic flux per plaquette, the Bloch eigenstates organize into topological bands characterized by non-zero Chern numbers [7]. The existence of finite energy gaps between these bands enables the exploration of nearly-flat band regimes that preserve the topological properties inherited by the Hofsdater eigenstates. The magnetic frustration can localize particles and modify the band structure, leading to the formation of nearly-flat magnetic sub-bands with non-zero Chern number. Therefore, in the nearly-flat limit, Hofstadter's bands effectively reproduce the Landau levels mechanism in 2D lattice electronic systems. Experimental realization of the Hofstadter Hamiltonian with ultracold atoms in optical lattices [24] represents a key step towards the controlled simulation of quantum Hall physics, providing the first direct implementation of topological bands in a synthetic lattice system. In this context, synthetic gauge fields arise not only as tools for inducing topological band structures with non-zero Chern number, but also enable the realization of correlation-driven phenomena in the nearly-flat regime [18, 19, 22].

Along this line, realizations of bosonic fractional quantum Hall states in optical lattices have been theoretically proposed [25–27], and first experimental signatures have been recently observed in few-particle systems [28]. In parallel, topologically non-trivial band structures without external magnetic fields [29] have been engineered in cold atom setups [30], providing a promising platform for exploring interacting topological phases [31, 32]. These synthetic topological bands typically possess non-zero Berry curvature and break time-reversal symmetry, enabling the observation of chiral dynamics and Hall-type responses in charge-neutral atomic systems.

An alternative strategy to break time-reversal symmetry without implementing generic gauge fields is to exploit the interplay of interactions and geometric frustration. In this context, π-flux lattices represent a prominent framework [33]. Introducing a half-flux quantum per unit cell induces frustration in the hopping dynamics. The corresponding interference induces localization and flat bands, where interactions play a dominant role.

In such systems π-flux induced degeneracies can emulate orbital physics in optical lattices, typically associated with higher Bloch bands, e.g. p-bands [34, 35]. It has been shown that interacting bosons in p-bands condense into complex superpositions of the orbital states and the resulting ground state may spontaneously break time-reversal symmetry [36, 37]. This generates effective angular momentum and vortex-like configurations in the condensate wavefunction [34, 38]. While quantum gases loaded into p-bands and higher bands suffer the limitation of their relatively short lifetime (typically of the order of a hundred milliseconds [38, 39]) due to atom-atom collisions, thus making it challenging to reach strongly interacting regimes, π-flux systems provide a shortcut to p-band orbital physics, which does not rely on populating higher bands.

This is the core idea of a recent theoretical study by Di Liberto and Goldman [35]. Based on the analogy between $p_{x,y}$ orbitals and the twofold degenerate low-energy orbitals provided by a square plaquette pierced by a π-flux, they show that interacting bosons on a 2D dimerized square lattice with π-flux can spontaneously break time-reversal symmetry and develop chiral orbital order over the extended lattice. In particular, in their work they demonstrate the emergence of a chiral superfluid vortex phase, exhibiting a long-lived gapped collective mode and local chiral currents. Moreover, for sufficiently strong interactions, the chiral superfluid undergoes a transition to a chiral Mott insulator for sufficiently strong interactions and half filling. Their model realizes an interacting bosonic version of the Benalcazar-Bernevig-Hughes (BBH) model [40], a minimal tight-binding lattice model firstly introduced in the context of higher-order topological insulators (HOTIs) in two and three dimensions. HOTIs are symmetry protected topological phases in dimensions $d > 1$, characterized by protected edge modes localized in $d - 2$ or lower dimensions. These properties are protected by crystalline symmetries and are characterized by quantized multipole moments, generalizing the bulk-boundary correspondence [40, 41].

Building upon this framework and motivated by recent experimental advances in two-dimensional bosonic systems [28, 42], this Thesis explores a three-dimensional extension of the model of Di Liberto and Goldman, based on frustrated cubic cells pierced by π-flux with Hubbard interactions. This setup defines a fully three-dimensional interacting bosonic BBH model, and the goal of this work is to understand whether 3D systems can also spontaneously break time-reversal symmetry. As we will see in the following chapters, we will positively answer this question.

Starting from the construction of the eight-site Bose-Hubbard Hamiltonian on the cubic unit cell pierced by a π-flux, we analyze how geometric frustration leads to a highly degenerate single-particle spectrum and affects lattice crystalline symmetry and their commutation relations. Grounded on this study, we derive an effective low-energy theory formulated in terms of a symmetry-adapted basis and investigate the presence of an emergent dynamical symmetry in the effective Hamiltonian. We show that the effective Hamiltonian can be recast into an algebraic form, which exhibits an emergent $SU(4)$ symmetry structure. This allows us to identify a natural organization of the theory in terms of Schwinger-type bilinears built from generators of the Lie algebra $\mathfrak{su}(4)$. We validate our theoretical results by performing exact diagonalization of the full Bose-Hubbard Hamiltonian on the π-flux cube, and comparing its energy spectrum with the one obtained from the projected theory. Remarkably, this analysis highlights the emergence of filling-dependent degeneracies and regular structures in the many-body energy spectrum, suggesting the presence of underlying hidden symmetries.

In the weakly interacting regime, we treat the problem using a discrete Gross-Pitaevskii description with N condensed particles, for both the full and the projected effective theory. Notably, we identify a highly degenerate classical ground-state manifold, characterized by the emergence of closed loop-current patterns related by time-reversal and crystalline lattice symmetries. These chiral modes spontaneously break time-reversal symmetry in the classical regime, hinting at the possibility of the emergence of intriguing three-dimensional many-body phases in the quantum limit.

The remainder of this Thesis is structured as follows. In Chapter 2, we review the bosonic version of the BBH model in two dimensions, revisiting the results of Ref. [35] for the π-flux square plaquette. We derive its effective low-energy theory within a symmetry-based approach, analyze the emergent p-orbital physics, and discuss the classical properties of the ground state within a Gross–Pitaevskii description. Finally, we discuss the analysis to the many-body physics of the 2D lattice assembled from coupled plaquettes. In Chapter 3, we present the three-dimensional bosonic BBH model, the model studied in this Thesis, and in Chapter 4 we discuss the numerical results. Finally, in Chapter 5 we draw the conclusions and outline possible directions and open questions for future studies.

2 The BBH Model

The Benalcazar–Bernevig–Hughes (BBH) model is a minimal tight-binding lattice model proposed to realize higher-order topological insulators (HOTIs) in two and three dimensions [40, 43]. Originally formulated for non-interacting spinless fermions on a square (2D) or cubic (3D) lattice, the BBH model is characterized by a gapped bulk and lower-dimensional boundary states. Lattice symmetries play a fundamental role in stabilizing its topological phases, characterized by quantized multipole moments. Differently from many crystalline topological insulators, e.g. the Su-Schrieffer-Heeger (SSH) model [44, 45], whose topology is characterized and classified by their bulk dipole, the BBH model exhibits quantized quadrupole or octupole moments depending on the dimensionality, and corner or hinge boundary modes.

The fermionic 2D BBH Hamiltonian is constructed from intra- and inter-unit cell nearest-neighbor hopping terms on a square lattice pierced by a magnetic π-flux (see Fig. 2.1), which in turn generates geometric frustration and induces strong degeneracies in the single-particle spectrum. The main effect of the magnetic flux is to give rise to a non-commuting nature of mirror symmetry operations, leading to a gapped band structure and quantization of the band quadrupole moment [43]. Importantly, the BBH model operates in a non-interacting framework, and the topological features are encoded entirely in the single-particle band structure. This makes it a paradigmatic platform for studying topological phenomena protected by crystalline symmetries, allowing for the investigation of more complex systems where interactions, disorder, or other perturbations are present.

Although originally formulated for non-interacting fermions, the structure of the BBH model enables to explore analogous bosonic systems, where the interplay between interactions and lattice symmetries opens new directions of

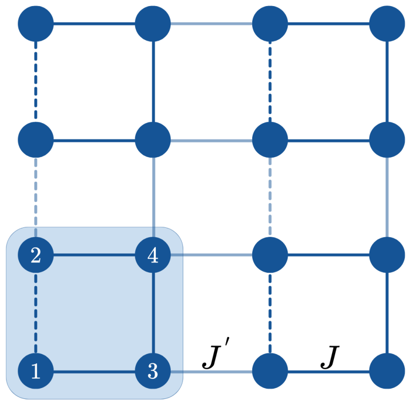

Figure 2.1: Geometry of the extended two-dimensional lattice, composed of π-flux plaquette building blocks (dark blue lines) coupled via weak interplaquette links $J' \ll J$ (light blue lines), preserving local orbital order and enabling the emergence of chiral many-body phases. Dashed lines denote the π-flux gauge choice.

research. In a recent work, Di Liberto and Goldman [35] introduce a bosonic version of the BBH model in two dimensions, embedding interacting bosons in a lattice of square plaquettes pierced by π-flux. Through a projection onto the lowest energy subspace, they derive an effective Hamiltonian in which the two degenerate low-energy modes mimic the behavior of bosons occupying p-orbitals: in the weakly interacting regime, the frustrated square plaquette hosts emergent p_x and p_y orbital-like degrees of freedom on each lattice site. In particular, the projected Hamiltonian is found to favor states with nonzero angular momentum L_z, namely a finite loop current in each plaquette, similar to the orbital ordering observed in p-band optical lattices, where bosons condense into chiral superpositions of p_x and p_y orbitals [34, 38, 46–48].

In analogy with the physics of bosons in p-bands [36], the nonzero angular momentum operator L_z plays a central role in driving the system into chiral phases that spontaneously break time-reversal symmetry. In the weakly interacting regime, the system forms a chiral superfluid vortex lattice, exhibiting long-range phase coherence and local chiral currents. As interactions increase, the system undergoes a transition to a chiral Mott insulator, characterized by finite local angular momentum but global incompressibility, meaning that the total density resists changes under variations of the chemical potential. The bosonic BBH model thus provides a route to explore chiral orbital order without requiring the physical population of higher Bloch bands, which are typically short-lived due to collisional instabilities in cold atom systems [38, 47].

An essential aspect of the frustrated lattice is how the π-flux modifies the symmetry structure, inducing a non-Abelian character in lattice symmetries, which tightly constrains the effective theory and enables a non-trivial symmetry-based approach. By constructing the low-energy Hamiltonian in a symmetric basis, one can reinterpret the emergent degrees of freedom in terms of SU(2) Schwinger bosons, offering a symmetry-resolved description that aligns with the physical intuition drawn from the orbital interpretation.

In this Chapter, we revisit the results in Ref. [35] by applying a symmetry-based approach to the two-dimensional bosonic BBH model, showing how the same p-orbital physics naturally emerges from symmetry properties of the model. The validity of the projected theory is established by comparing its spectrum to exact diagonalization of the full four-site plaquette Hamiltonian. We then study the classical properties of the ground state in the weakly-interacting regime by means of a Gross–Pitaevskii description, and numerically verify that the mean-field energy converges to the exact ground-state energy per particle in the thermodynamic limit. Finally, we discuss the many-body physics of the extended lattice, and outline the emergence of an effective ferro-orbital Hamiltonian that governs interplaquette coupling. This strategy also facilitates the analysis of the three-dimensional case, which is the main focus of this Thesis and is addressed in the next chapters.

2.1 Bosonic BBH model: the π-flux single plaquette

The BBH square plaquette pierced by a π-flux, shown in Fig. 2.2, is described by the single-particle hopping Hamiltonian

$$\hat{H}_0 = -J\left(e^{i\pi}\hat{b}_1^\dagger\hat{b}_2 + \hat{b}_2^\dagger\hat{b}_4 + \hat{b}_4^\dagger\hat{b}_3 + \hat{b}_3^\dagger\hat{b}_1 + \text{H.c.}\right), \tag{2.1}$$

where $\hat{b}_i^\dagger$ ($\hat{b}_i$) creates (annihilates) a boson on site i of the plaquette, and J is the hopping amplitude between nearest-neighbor sites. The factor $e^{i\pi} = -1$ reflects our gauge choice to account for the π-flux threading the plaquette, effectively introducing a negative sign in the hopping on one of the links, and thereby generating a non-trivial phase pattern that leads to geometric frustration.

We consider interacting bosonic particles, e.g. atoms in optical lattices, with on-site Bose-Hubbard interaction:

$$\hat{H}_{\text{int}} = \frac{U}{2}\sum_i \hat{n}_i(\hat{n}_i - 1), \tag{2.2}$$

where $\hat{n}_i = \hat{b}_i^\dagger\hat{b}_i$ is the number operator on site i, and $U > 0$ denotes repulsive

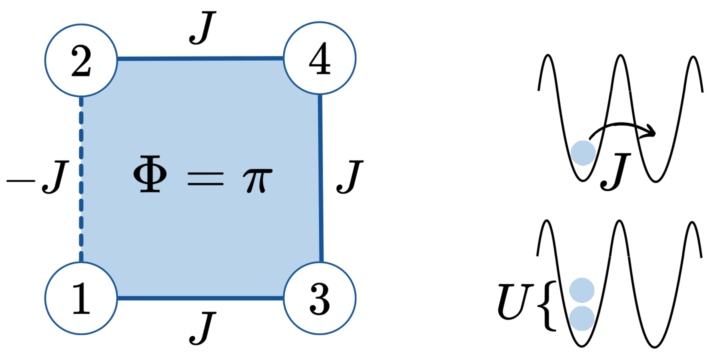

Figure 2.2: Geometry of the single plaquette, with hopping amplitude J (solid lines) and a π-flux (dashed line) threading the unit cell. The right panel illustrates the hopping process J and the on-site interaction U, for bosonic particles.

interactions. The full Hamiltonian thus reads:

$$\hat{H} = \hat{H}_0 + \hat{H}_{\text{int}} \,. \tag{2.3}$$

The single-particle spectrum of the π-flux plaquette is shown in Fig. 2.3 and consists of two pairwise degenerate eigenstates. Two low-energy modes with eigenvalues $\varepsilon_{1,2} = -\sqrt{2}J$ and two high-energy modes with $\varepsilon_{3,4} = +\sqrt{2}J$, are separated by a finite energy gap controlled by the hopping amplitude J.

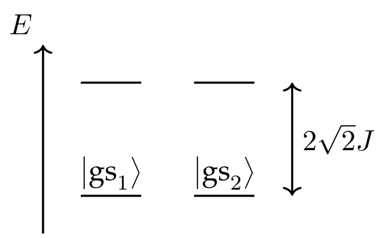

Figure 2.3: Single-particle spectrum displaying two-fold degeneracy separated by an energy gap $\Delta\varepsilon = 2\sqrt{2}J$. The degenerate states $|\mathrm{gs}_1\rangle$ and $|\mathrm{gs}_2\rangle$ span the low-energy subspace relevant for constructing the effective theory.

2.2 A symmetry-based approach

To construct an effective theory grounded in symmetry principles and to explicitly connect the emergent p-band physics to the crystalline symmetries of the model, we begin by analyzing the mirror symmetries of the square unit cell. Specifically, we focus on the reflection symmetries M_x and M_y along the two central axes of the plaquette, as shown in Fig. 2.4. We represent each mirror transformation as a unitary operator, $\hat{M}_x$ and $\hat{M}_y$, acting on the single-particle Hilbert space spanned by the $\{|b_i\rangle\}$. For these operators, we construct explicit

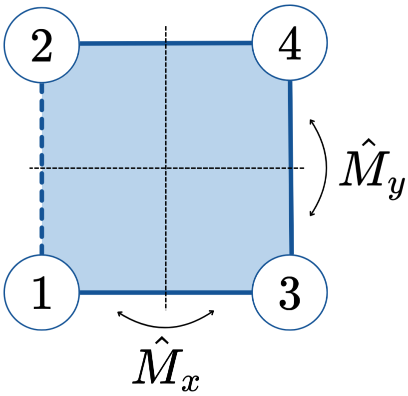

Figure 2.4: Mirror symmetries of the single square plaquette. $\hat{M}_y$ and $\hat{M}_x$ represent mirror transformations across the $y = 0$ and $x = 0$ axes, respectively, upon which we construct the symmetry-based effective description.

matrix representations in the four-dimensional space of the plaquette sites and we show how their commutation relations are modified by the presence of the magnetic flux.

Mirror symmetry along the $y = 0$ axis

Reflection across the axis $y = 0$ acts on the plaquette degrees of freedom as:

$$\hat{M}_y^0 \begin{pmatrix} \hat{b}_1 \\ \hat{b}_2 \\ \hat{b}_3 \\ \hat{b}_4 \end{pmatrix} (\hat{M}_y^0)^{-1} = \begin{pmatrix} \hat{b}_2 \\ \hat{b}_1 \\ \hat{b}_4 \\ \hat{b}_3 \end{pmatrix}, \tag{2.4}$$

and is represented by $\hat{M}_y^0 = \sigma^0 \otimes \sigma^x$, where σ^α with $\alpha = x, y, z$ are the Pauli matrices and σ^0 denotes the 2×2 identity matrix. This mirror operation is such that $[\hat{M}_y^0, \hat{H}_0] = 0$, thus representing a symmetry of the system. This holds because, in our gauge choice, the π-flux configuration introduces a minus sign in the hopping along one vertical link, and reflection across y does not alter the overall phase pattern.

Mirror symmetry along the $x = 0$ axis

Reflection across the $x = 0$ axis acts as:

$$\hat{M}_x^0 \begin{pmatrix} \hat{b}_1 \\ \hat{b}_2 \\ \hat{b}_3 \\ \hat{b}_4 \end{pmatrix} (\hat{M}_x^0)^{-1} = \begin{pmatrix} \hat{b}_3 \\ \hat{b}_4 \\ \hat{b}_1 \\ \hat{b}_2 \end{pmatrix}, \tag{2.5}$$

and is represented by $\hat{M}_x^0 = \sigma^x \otimes \sigma^0$. However, this transformation is not strictly a symmetry for the π-flux square plaquette: applying $\hat{M}_x^0$ modifies the flux threading the plaquette, altering the phase structure of the hopping terms by moving the negative sign from the 1–2 bond to the 3–4 one. This leads to:

$$[\hat{M}_x^0, \hat{H}_0] \neq 0\,. \tag{2.6}$$

To restore symmetry, we must dress the transformation by a gauge factor that compensates for the phase change [43]. We introduce the gauge choice $\hat{\mathcal{G}}^{(M_x)} = \sigma^0 \otimes \sigma^z$, so that the gauge-dressed mirror operation becomes:

$$\hat{M}_x = \hat{\mathcal{G}}^{(M_x)} \hat{M}_x^0 = \sigma^x \otimes \sigma^z\,, \tag{2.7}$$

which now satisfies:

$$\hat{M}_x \hat{H}_0 \hat{M}_x^{-1} = \hat{H}_0, \quad [\hat{M}_x, \hat{H}_0] = 0\,. \tag{2.8}$$

A crucial consequence of introducing a magnetic flux is that it forces the crystalline symmetries to become non-Abelian: while $\hat{M}_x^0$ and $\hat{M}_y^0$ would commute in a flux-free system, here their gauge-dressed counterparts satisfy:

$$[\hat{M}_x, \hat{M}_y^0] = -2i\, \sigma^x \otimes \sigma^y\,, \tag{2.9}$$

while now they anticommute:

$$\{\hat{M}_x, \hat{M}_y^0\} = 0\,. \tag{2.10}$$

These facts are behind the non-trivial quadrupolar topology of the BBH model [43].

2.3 Effective theory in mirror basis

Upon describing the crystalline mirror symmetries of the square plaquette, we are now ready to formulate the effective theory in the symmetry eigenspace of the system. Since mirror operations do not commute in the gauge-dressed form, only one can be diagonalized simultaneously with the single-particle Hamiltonian. Without loss of generality (the procedure is equivalent if the gauge-dressed x-reflection is chosen), we focus on the y-mirror operator $\hat{M}_y^0$.

By diagonalizing $\hat{M}_y^0$ together with the single-particle Hamiltonian $\hat{H}_0$, we obtain a set of common eigenvectors defined by

$$|b_i\rangle = \sum_j \mathcal{U}_{ij} \; |m_j\rangle \,, \tag{2.11}$$

where $\mathcal{U}_{ij}$ are the elements of the unitary matrix that simultaneously diagonalizes $\hat{M}_y^0$ and $\hat{H}_0$:

$$\hat{\mathcal{U}} = \frac{1}{2\sqrt{2}} \begin{pmatrix} -\frac{1-\sqrt{2}}{\sqrt{2-\sqrt{2}}} & -\frac{1+\sqrt{2}}{\sqrt{2+\sqrt{2}}} & \frac{1}{\sqrt{2-\sqrt{2}}} & \frac{1}{\sqrt{2+\sqrt{2}}} \\ \frac{1-\sqrt{2}}{\sqrt{2-\sqrt{2}}} & \frac{1+\sqrt{2}}{\sqrt{2+\sqrt{2}}} & \frac{1}{\sqrt{2-\sqrt{2}}} & \frac{1}{\sqrt{2+\sqrt{2}}} \\ -\frac{1}{\sqrt{2-\sqrt{2}}} & -\frac{1}{\sqrt{2+\sqrt{2}}} & \frac{1-\sqrt{2}}{\sqrt{2-\sqrt{2}}} & \frac{1+\sqrt{2}}{\sqrt{2+\sqrt{2}}} \\ \frac{1}{\sqrt{2-\sqrt{2}}} & \frac{1}{\sqrt{2+\sqrt{2}}} & \frac{1-\sqrt{2}}{\sqrt{2-\sqrt{2}}} & \frac{1+\sqrt{2}}{\sqrt{2+\sqrt{2}}} \end{pmatrix} . \tag{2.12}$$

The eigenstates $|m_j\rangle$ are thus labeled by two quantum numbers: the energy eigenvalue ε_j and the mirror eigenvalue $m_{y,j}$, associated with $\hat{H}_0$ and $\hat{M}_y^0$, respectively. We define the operators $\hat{m}_i$ corresponding to the symmetry eigenstates via:

$$\hat{b}_i = \sum_j \mathcal{U}_{ij} \; \hat{m}_j \,, \tag{2.13}$$

and rewrite the full Hamiltonian in terms of $\hat{m}_i$ bosonic operators, in a form that explicitly conserves y-reflection symmetry.

In the regime where the on-site interaction strength U is much smaller than the energy gap $\Delta\varepsilon = 2\sqrt{2}J$ (see Fig. 2.3), the system's low-energy dynamics can be effectively captured by projecting the full Hamiltonian onto the two-fold degenerate ground-state manifold. We thus consider the projected Hamiltonian

$$\hat{H}_{\text{eff}} = \hat{\mathcal{P}} \hat{H} \hat{\mathcal{P}}, \tag{2.14}$$

where $\hat{\mathcal{P}}$ is the projection operator onto the low-energy subspace spanned by the two degenerate ground states $\{|m_1\rangle, |m_2\rangle\}$. In this projected space, the interacting part of the effective Hamiltonian reads

$$\begin{aligned} \hat{H}_{\text{eff}}^{\text{int}} = \frac{3U}{16}\Big(\hat{m}_1^\dagger \hat{m}_1^\dagger \hat{m}_1 \hat{m}_1 + \hat{m}_2^\dagger \hat{m}_2^\dagger \hat{m}_2 \hat{m}_2\Big) + \frac{U}{4} \hat{m}_1^\dagger \hat{m}_2^\dagger \hat{m}_1 \hat{m}_2 \\ + \frac{U}{16}\Big(\hat{m}_1^\dagger \hat{m}_1^\dagger \hat{m}_2 \hat{m}_2 + \hat{m}_2^\dagger \hat{m}_2^\dagger \hat{m}_1 \hat{m}_1\Big), \end{aligned} \tag{2.15}$$

which has the same form as the projected Hamiltonian in Ref. [35].

To gain further insight into the effective Hamiltonian in Eq. (2.15), we rely on the formalism of the Jordan-Schwinger map, which establishes a direct mapping

between Lie algebra representations and bosonic modes [49–51]. To this end, we adopt the $SU(2)$ structure, which provides a complete basis for all possible Hermitian operators acting on the two-dimensional low-energy subspace.
Following the general framework presented in Ref. [51], we construct the $SU(2)$ Schwinger boson operators in the projected space, whose explicit derivation is provided in Appendix A. These operators are expressed in terms of the two low-energy modes as:

$$\begin{aligned}
\hat{J}_x &= \frac{1}{2}\left(\hat{m}_1^\dagger \hat{m}_2 + \hat{m}_2^\dagger \hat{m}_1\right), \\
\hat{J}_y &= \frac{1}{2i}\left(\hat{m}_1^\dagger \hat{m}_2 - \hat{m}_2^\dagger \hat{m}_1\right), \\
\hat{J}_z &= \frac{1}{2}\left(\hat{m}_1^\dagger \hat{m}_1 - \hat{m}_2^\dagger \hat{m}_2\right).
\end{aligned} \tag{2.16}$$

In this representation, we can express the effective Hamiltonian solely in terms of the total particle number operator, $\hat{n} = \hat{m}_1^\dagger \hat{m}_1 + \hat{m}_2^\dagger \hat{m}_2$, its square, $\hat{n}^2$, and the square of the angular momentum operator along the y-direction, $\hat{J}_y^2$:

$$\hat{H}_{\text{eff}} = \frac{3U}{16}\hat{n}^2 - \left(\sqrt{2}J + \frac{U}{8}\right)\hat{n} - \frac{U}{4}\hat{J}_y^2 . \tag{2.17}$$

Here, $\hat{J}_y$ plays the role of the effective angular momentum $\hat{L}_z$ introduced in Ref. [35], with the difference in the numerical prefactor arising from the normalization choice in the definition in $SU(2)$ Schwinger operators.
Since $[\hat{n}, \hat{J}_y] = 0$, we can express the eigenstates of $\hat{H}_{\text{eff}}$ in terms of the single-particle eigenstates of $\hat{J}_y$:

$$|m^\pm\rangle \equiv \hat{m}_\pm^\dagger |0\rangle , \tag{2.18}$$

such that $\hat{J}_y |m^\pm\rangle = \pm\frac{1}{2} |m^\pm\rangle$, where we define the complex orbital operators

$$\hat{m}_\pm^\dagger = \frac{1}{\sqrt{2}}(\hat{m}_1^\dagger \pm i\hat{m}_2^\dagger), \tag{2.19}$$

acting on the vacuum state $|0\rangle$ with zero boson occupation, and creating a particle in the state with angular momentum $\pm\frac{1}{2}$.

Many-body eigenstates of the low-energy Hamiltonian, with n_+ bosons in the state $|m^+\rangle$ and n_- bosons in the state $|m^-\rangle$, can be written as

$$|n_+, n_-\rangle = \frac{1}{\sqrt{n_+! n_-!}}(\hat{m}_+^\dagger)^{n_+}(\hat{m}_-^\dagger)^{n_-} |0\rangle , \tag{2.20}$$

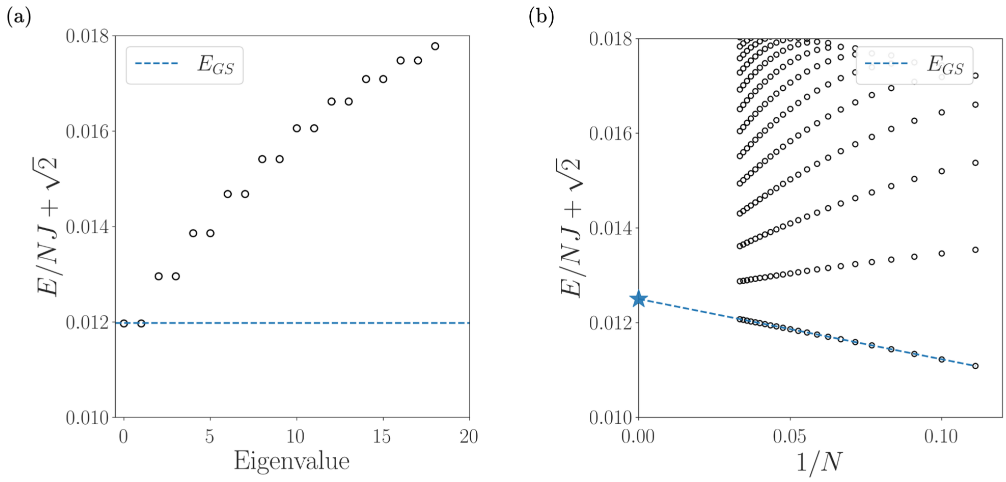

Figure 2.5: Energy spectrum of the four-site plaquette Hamiltonian obtained via exact diagonalization, for $g = UN = 0.1J$. (a) Spectrum at fixed $N = 24$, showing how the emergence of $\mathbb{Z}_2$ symmetry manifests as a twofold degeneracy in the eigenstates. The dashed line marks the analytical values of the effective ground-state energy E_{GS}. (b) Energy per particle E/N as a function of inverse particle number $1/N$. The analytical ground-state energy E_{GS} shows close agreement with the full theory, and corresponds to the mean-field result, represented by the blue star, in the limit $N \to \infty$.

where since $\hat{n} = \hat{m}_1^\dagger \hat{m}_1 + \hat{m}_2^\dagger \hat{m}_2 = \hat{m}_+^\dagger \hat{m}_+ + \hat{m}_-^\dagger \hat{m}_-$,

$$\begin{aligned} \hat{n}\,|n_+, n_-\rangle &= \left(\hat{m}_+^\dagger \hat{m}_+ + \hat{m}_-^\dagger \hat{m}_-\right)|n_+, n_-\rangle \\ &= (n_+ + n_-)\,|n_+, n_-\rangle \\ &= N\;|n_+, n_-\rangle\,. \end{aligned} \tag{2.21}$$

with N the total number of particles.

The energy spectrum of the projected theory is given by

$$E_{\text{eff}}(n_+, n_-) = \frac{3U}{16}N^2 - \frac{U}{16}(n_+ - n_-)^2 - \left(\sqrt{2}J + \frac{U}{8}N\right). \tag{2.22}$$

Besides the conservation of total particle number, the projected low-energy theory also features an emergent discrete $\mathbb{Z}_2$ symmetry, as arising from the invariance of the effective Hamiltonian in Eq. (2.15) under the exchange of the two low-energy modes: $\hat{m}_1 \leftrightarrow \hat{m}_2$. This transformation inverts the sign of the angular momentum operator, $\hat{J}_y \to -\hat{J}_y$, and hence maps each eigenstate $|n_+, n_-\rangle$ to its chiral counterpart. The emergent $\mathbb{Z}_2$ symmetry is also captured by the two-fold degeneracy of the full theory energy spectrum, as shown in Fig. 2.5.

Crucially, the term $-\frac{U}{4}\hat{J}_y^2$ in Eq. (2.17) energetically favors plaquette configurations with maximal angular momentum, leading to a macroscopic occupation of the complex orbital $|m^{\pm}\rangle$ in the ground state, corresponding to $n_+ = N$ or $n_- = N$. The resulting two-fold degenerate many-body ground state

$$\left|\psi^{\pm}_{\mathrm{GS}}\right\rangle \sim (\hat{m}_1^\dagger \pm i\hat{m}_2^\dagger)^N |0\rangle , \tag{2.23}$$

is a chiral orbital condensate with angular momentum $\langle \hat{J}_y \rangle = \pm \frac{N}{2}$, analogous to the macroscopic occupation of $p_x \pm ip_y$ orbitals in optical lattices, and ground state energy per particle given by

$$\frac{E_{\mathrm{GS}}}{N} = \frac{U}{8}N - \sqrt{2}J - \frac{U}{8} . \tag{2.24}$$

Comparison with the four-site plaquette energy spectrum in Fig. 2.5 shows how the projected theory carefully reproduces the low-energy physics of the model in the weakly interacting limit.

As in systems of bosons occupying p_x and p_y orbitals, where angular momentum arises from coherent superpositions of the form $\hat{p}_x \pm i\hat{p}_y$ [34, 38, 46], the operators $\hat{m}_\pm$ in the projected basis act as complex orbitals whose population defines an effective angular momentum of the condensate. Indeed, such wavefunction is complex, thus reflecting time-reversal symmetry breaking. This corresponds to a non-vanishing loop current for the plaquette defined as

$$\hat{\mathcal{L}} = i\left(\hat{b}_1^\dagger \hat{b}_3 + \hat{b}_3^\dagger \hat{b}_4 + \hat{b}_4^\dagger \hat{b}_2 - \hat{b}_2^\dagger \hat{b}_1 - \mathrm{H.c.}\right) , \tag{2.25}$$

which, in the projected space, results proportional to the effective angular momentum operator:

$$\hat{\mathcal{L}} \approx 2\sqrt{2}\hat{J}_y, \tag{2.26}$$

implying a finite ground-state expectation value.

2.4 Classical properties of the ground state

We further investigate the properties of the chiral ground state from the classical point of view by constructing a mean-field Gross–Pitaevskii theory for N condensed particles in the weak interacting regime. For finite $g \equiv UN$, with $U \to 0$ and in the thermodynamic limit $N \to \infty$, we can replace the bosonic operators in Eq. (2.15) with their classical coherent state expectation value, for which we make the *ansatz*

$$\hat{m}_1 \to \langle \hat{m}_1 \rangle = \sqrt{N_1} , \quad \hat{m}_2 \to \langle \hat{m}_2 \rangle = \sqrt{N_2} e^{i\theta} , \tag{2.27}$$

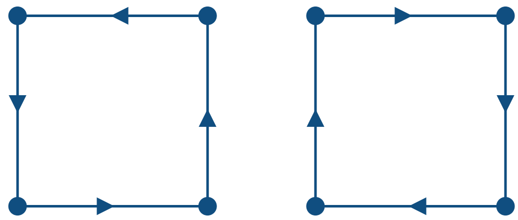

Figure 2.6: Loop current configurations corresponding to the two degenerate classical ground states, with currents flowing in the plaquette in opposite directions and corresponding to the values $\pm\sqrt{2}N$.

where we have exploited the gauge freedom provided by the global $U(1)$ symmetry and fixed the phase of $\langle\hat{m}_1\rangle$ to zero. With these assumptions, the angular momentum operator leads to

$$\hat{J}_y = \frac{1}{2i}\left(\hat{m}_1^\dagger\hat{m}_2 - \hat{m}_2^\dagger\hat{m}_1\right) \to \sqrt{N_1 N_2}\sin\theta\,. \tag{2.28}$$

The mean field energy functional thus yields

$$E_{\mathrm{MF}}[m_1, m_2] = E(N) - \frac{U}{4}N_1(N-N_1)\sin^2\theta\,, \tag{2.29}$$

where $E(N) = \frac{3U}{16}N^2 - \left(\sqrt{2}+\frac{U}{8}\right)N$. This energy functional is minimized for $N_{1,2} = \frac{N}{2}$ and $\theta = \pm\frac{\pi}{2}$, corresponding to two discrete and degenerate minima reflecting time-reversal symmetry. In the thermodynamic limit, the system spontaneously selects one of the two ground states, thereby breaking time-reversal symmetry. In particular, the two degenerate ground states correspond to opposite values of the mean-field angular momentum in Eq. (2.28). This implies two non-vanishing opposite values of the classical loop current

$$\mathcal{L} = 2\sqrt{2N_1N_2}\sin\theta, \tag{2.30}$$

in the ground state, corresponding to the two configurations in Fig. 2.6. As already revealed by the effective theory result in Eq. (2.26), the degenerate ground state is characterized by the emergence of chiral currents defining closed-loop patterns. The two configurations are related by time-reversal symmetry, with current flowing in the square plaquette in opposite directions and corresponding to the values $\pm\sqrt{2}N$.

At last, we observe that the mean field ground state energy per particle of these configurations

$$\frac{E_{\mathrm{GS}}^{\mathrm{MF}}}{N} = -\sqrt{2}J + \frac{g}{8}\,, \tag{2.31}$$

agrees with the effective energy per particle in Eq. (2.24) obtained within the projected theory, in the limit $N \to \infty$:

$$\frac{E_{\text{GS}}}{N} = -\sqrt{2}J + \frac{g}{8} - \frac{g}{8N} \xrightarrow{N\to\infty} -\sqrt{2}J + \frac{g}{8}\,, \tag{2.32}$$

as highlighted in Fig. 2.5.

2.5 Orbital order over the extended lattice

As the last step in our treatment of the two-dimensional model, we address the many-body physics of the system by assembling the π-flux building blocks into an extended lattice, and show how the chiral properties of single plaquettes give rise to chiral phases of matter. Coupling them with weak links $J^{'} \ll J$ preserves the local orbital order, so that each plaquette acts as a supersite effectively hosting two orbital degrees of freedom, resembling the structure of p-band models in optical lattices.

Indicating with $\mathbf{r}$ the position of the (plaquette) unit cell, and with i the sublattice (plaquette site) index, the interaction among different plaquettes in the square geometry in Fig. 2.1 is described by

$$\hat{H}^{(\text{inter})} = -J^{'} \sum_{\mathbf{r}} \left(e^{i\pi} \hat{b}^{\dagger}_{1,\mathbf{r}+\mathbf{e_y}} \hat{b}_{2,\mathbf{r}} + \hat{b}^{\dagger}_{3,\mathbf{r}+\mathbf{e_y}} \hat{b}_{4,\mathbf{r}} + \hat{b}^{\dagger}_{1,\mathbf{r}+\mathbf{e_x}} \hat{b}_{3,\mathbf{r}} + \hat{b}^{\dagger}_{2,\mathbf{r}+\mathbf{e_x}} \hat{b}_{4,\mathbf{r}} + \text{H.c.} \right),$$

where $\mathbf{e_x} = (a, 0)$, $\mathbf{e_y} = (0, a)$, and a is the lattice constant.

Using the unitary transformation $\hat{\mathcal{U}}$ in Eq. (2.12), we rewrite the interplaquette Hamiltonian in the symmetric basis defined by $\hat{b}_i = \sum_j \mathcal{U}_{ij} \hat{m}_j$. Upon projection onto the single-plaquette lowest-energy subspace, we obtain

$$\begin{aligned}
\hat{H}^{(\text{inter})}_{\text{eff}} &= \hat{\mathcal{P}} \hat{H}^{(\text{inter})} \hat{\mathcal{P}} \\
&= -J' \sum_{\mathbf{r}} \Big[e^{i\pi} (\mathcal{U}_{12} \hat{m}^{\dagger}_{1,\mathbf{r}+\mathbf{e_y}} + \mathcal{U}_{14} \hat{m}^{\dagger}_{2,\mathbf{r}+\mathbf{e_y}}) (\mathcal{U}_{22} \hat{m}_{1,\mathbf{r}} + \mathcal{U}_{24} \hat{m}_{2,\mathbf{r}}) \\
&\qquad + (\mathcal{U}_{32} \hat{m}^{\dagger}_{1,\mathbf{r}+\mathbf{e_y}} + \mathcal{U}_{34} \hat{m}^{\dagger}_{2,\mathbf{r}+\mathbf{e_y}}) (\mathcal{U}_{42} \hat{m}_{1,\mathbf{r}} + \mathcal{U}_{44} \hat{m}_{2,\mathbf{r}}) \\
&\qquad + (\mathcal{U}_{12} \hat{m}^{\dagger}_{1,\mathbf{r}+\mathbf{e_x}} + \mathcal{U}_{14} \hat{m}^{\dagger}_{2,\mathbf{r}+\mathbf{e_x}}) (\mathcal{U}_{32} \hat{m}_{1,\mathbf{r}} + \mathcal{U}_{34} \hat{m}_{2,\mathbf{r}}) \\
&\qquad + (\mathcal{U}_{22} \hat{m}^{\dagger}_{1,\mathbf{r}+\mathbf{e_x}} + \mathcal{U}_{24} \hat{m}^{\dagger}_{2,\mathbf{r}+\mathbf{e_x}}) (\mathcal{U}_{42} \hat{m}_{1,\mathbf{r}} + \mathcal{U}_{44} \hat{m}_{2,\mathbf{r}}) + \text{H.c} \Big].
\end{aligned} \tag{2.33}$$

Here, the eigenvectors associated with the low-energy eigenvalue $\varepsilon = -\sqrt{2}J$ correspond to the second and fourth columns of the matrix $\hat{\mathcal{U}}$, and $\hat{m}_{1,2}$ are the projected orbital operators acting on each plaquette.

By substituting the values of the matrix elements (2.12), the interplaquette

Hamiltonian in the projected space takes the form

$$\hat{H}_{\text{eff}}^{(\text{inter})} = -\frac{J'}{\sqrt{2}} \sum_{\mathbf{r},\sigma,\nu} \left(\hat{m}^{\dagger}_{\sigma,\mathbf{r}+\mathbf{e}_\nu} \hat{m}_{\sigma,\mathbf{r}} + \text{H.c} \right) . \tag{2.34}$$

Differently from higher bands physics in cold atoms, the effective tunneling coupling (2.34) is ferromagnetic and isotropic in all directions [35, 38].

Dynamics within each plaquette is described by the local term

$$\hat{H}_{\text{eff}}^{(\text{plaq})} = \sum_{\mathbf{r}} \Big[\frac{3U}{16} \hat{n}_{\mathbf{r}}^2 - \Big(\sqrt{2}J + \frac{U}{8} \Big) \hat{n}_{\mathbf{r}} - \frac{U}{4} \hat{J}_{y,\mathbf{r}}^2 \Big] , \tag{2.35}$$

so that the Hamiltonian for the extended lattice is given by

$$\hat{H}_{\text{eff}} = \hat{H}_{\text{eff}}^{(\text{plaq})} + \hat{H}_{\text{eff}}^{(\text{inter})} . \tag{2.36}$$

The low-energy many-body physics is thus described by a ferromagnetic Hamiltonian ($J^{'} > 0$) that favors configurations in which bosons at different sites occupy the same complex orbital, thus maximizing the angular momentum. This ferro-orbital interaction leads to the emergence of a chiral superfluid vortex lattice, exhibiting a long-lived gapped collective mode that is characterized by local chiral currents [35]. In Ref. [35], the authors explore the consequences of this resulting chiral orbital order, both for weak and strong on-site interactions, and demonstrate that the chiral superfluid phase undergoes a phase transition to a chiral Mott insulator for sufficiently strong interactions, offering the opportunity to observe chiral bosonic phases in the strongly correlated regime.

3 The 3D BBH Model

Having established the background for the two-dimensional square plaquette, in this Chapter we introduce and study the three-dimensional bosonic BBH model, the principal focus of this Thesis.

We develop the theory for the frustrated Bose–Hubbard model on a single cubic cell starting from the construction of the full tight-binding Hamiltonian for the eight-site unit cell in the presence of a π-flux piercing the cube. Upon identifying its single-particle spectrum we construct a symmetry-based effective theory by performing a detailed analysis of the crystalline symmetries of the cube. The presence of synthetic flux requires us to consider the gauge structure necessary to restore the invariance of the Hamiltonian under these symmetries, which in turn constrains their algebra. Based on this analysis, we construct a symmetry-adapted single-particle basis labeled by crystalline quantum numbers and derive an effective low-energy theory that captures the physics of the degenerate ground-state manifold in the weakly interacting regime. We classify the interaction terms in the effective Hamiltonian according to their effect on the mirror and rotation sectors and reveal the emergence of additional internal symmetries in the effective theory.

To further understand the structure of the interactions, we investigate the presence of an emergent dynamical symmetry, also referred to as a spectrum-generating algebra. Recasting the Hamiltonian in an algebraic form using generalized Schwinger bilinear operators, we develop an algebraic description of the effective theory in terms of an algebra representation. This reformulation reveals an underlying algebraic structure and leads to the identification of an emergent $SU(4)$ dynamical symmetry.

The analysis developed in this Chapter is a first step toward the characterization of the low-energy physics of the single π-flux cubic cell in the weakly

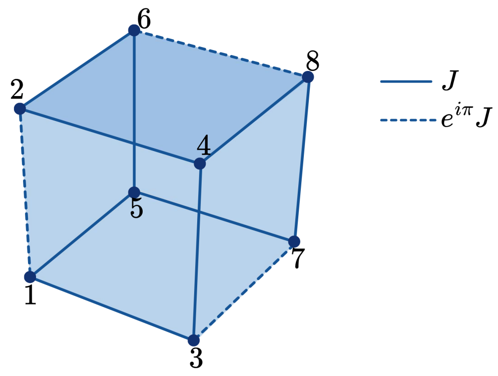

Figure 3.1: Geometry and gauge choice of the 3D lattice model, with a flux $\Phi = \pi$ threading each face of the cubic unit cell. Solid lines correspond to hopping amplitude J, and dashed lines to $-J$.

interacting regime.

3.1 The π-flux cubic cell

Our starting point is the single cubic cell described by the Bose–Hubbard Hamiltonian as in Eq. (2.3)

$$\hat{H} = \sum_{\langle ij \rangle} J_{ij}\, \hat{b}_i^\dagger \hat{b}_j + \frac{U}{2}\sum_i \hat{n}_i(\hat{n}_i - 1)\,, \tag{3.1}$$

where J_{ij} is the nearest-neighbor hopping amplitude between the sites i and j of the eight-site unit cell. Each face of the cube is threaded by half flux quantum $\Phi = \pi$ and in our gauge choice (see Fig. 3.1), the hopping terms explicitly read:

$$\begin{aligned} \hat{H}_0 = -J(&e^{i\pi} b_1^\dagger b_2 + b_2^\dagger b_4 + b_4^\dagger b_3 + b_3^\dagger b_1 + b_7^\dagger b_8 + e^{i\pi} b_8^\dagger b_6 \\ &+ b_6^\dagger b_5 + b_5^\dagger b_7 + e^{i\pi} b_7^\dagger b_3 + b_5^\dagger b_1 + b_4^\dagger b_8 + b_2^\dagger b_6 + \text{H.c}\,). \end{aligned} \tag{3.2}$$

As in the case of the two-dimensional square plaquette, flux-induced frustration leads to a degenerate single-particle spectrum, shown in Fig. 3.2, consisting of a four-fold degenerate ground state, with energy $\varepsilon_- = -\sqrt{3}J$ and an equally degenerate first excited states sector with energy $\varepsilon_+ = \sqrt{3}J$.

In the weakly interacting regime, the energy gap $\Delta\varepsilon = 2\sqrt{3}J \gg U$ allows for the construction of a low-energy effective theory by projection onto the four-fold ground-state manifold. To this end, and following the approach used for the 2D plaquette, a preliminary step is to characterize the crystalline symmetries of the cubic cell.

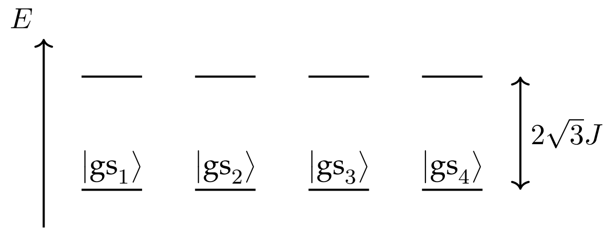

Figure 3.2: Single-particle spectrum of the π-flux cubic cell, exhibiting a four-fold degenerate ground state separated by an equally degenerate excited state by a finite energy gap $\Delta\varepsilon = 2\sqrt{3}J$.

3.2 Crystalline symmetries of the cubic cell

To construct a symmetry-based effective theory, we perform a detailed analysis of the crystalline symmetries of the cubic cell pierced by a π-flux. As in the two-dimensional case, the presence of magnetic flux constrains the algebra of symmetry operations, requiring a gauge-dressed formulation to recover the invariance of the Hamiltonian under spatial transformations.

In this Section, we focus on the following set of spatial symmetries:

- Reflection symmetries across the three principal planes $x = 0$, $y = 0$, $z = 0$, denoted as M_x, M_y and M_z, respectively,
- Rotational symmetries by angles π around the x, y, and z axes, which we denote $C_{2,x}$, $C_{2,y}$ and $C_{2,z}$,
- Inversion symmetry $\mathcal{I}$ with respect to the center of the cube.

In addition, we notice that the cubic cell also exhibits (gauge-dressed) $\pi/2$-rotational symmetries $C_{4,\alpha}$ about the three principal axes $\alpha = x, y, z$. Since they are not directly employed in the following analysis, we will not report them explicitly here, but it is worth mentioning them as we will encounter them in the next Chapter.

Each symmetry is represented by a unitary operator acting on the eight-site basis of the cubic cell, whose vertex indexing is illustrated in Fig. 3.1. While the geometric action of each symmetry is a permutation of site indices, the presence of the π-flux implies that such operations generally do not leave the single-particle Hamiltonian $\hat{H}_0$ invariant. However, invariance can be restored by composing the symmetry operations with an appropriate gauge transformation. Below we detail each case. We will explicitly construct the matrix representations of these operations, identify the necessary gauge dressing, and determine the algebra they satisfy. In particular, we are interested in identifying which pairs of dressed symmetry operators commute or generate new symmetry operations under composition. This analysis is essential for constructing a symmetry-adapted basis in the next Section.

3.2.1 Mirror symmetries

We start by considering the mirror symmetries of the cubic cell, corresponding to discrete spatial reflections across the three principal planes. Each transformation is represented by a permutation matrix acting on the eight-dimensional single-particle Hilbert space $\{|b_i\rangle\}$, with $i = 1, \ldots, 8$. In particular, these can be written in terms of Pauli matrices σ^μ (see Ref. [43]) as

$$\begin{aligned} \hat{M}_x^0 &= \sigma^x \otimes \sigma^0 \otimes \sigma^0, \\ \hat{M}_y^0 &= \sigma^0 \otimes \sigma^x \otimes \sigma^0, \\ \hat{M}_z^0 &= \sigma^0 \otimes \sigma^0 \otimes \sigma^x. \end{aligned} \tag{3.3}$$

Mirror operations exchange sites across the perpendicular axis to the corresponding plane, while leaving coordinates along the other two axes invariant. While operators $\hat{M}_\alpha^0$ correctly permute the site labels, in the presence of a π-flux, the geometric action of these reflections alters the pattern of complex hopping amplitudes. Moving the negative sign in the hopping to different bonds, bare mirror operations don't leave the single-particle Hamiltonian invariant:

$$[\hat{M}_\alpha^0, \hat{H}_0] \neq 0, \quad \alpha = x, y, z. \tag{3.4}$$

However, symmetry can be restored via suitable gauge transformations. For each mirror operation, we consider a diagonal gauge operator

$$\begin{aligned} \hat{\mathcal{G}}^{(M_x)} &= \mathrm{diag}(1, -1, 1, 1, 1, -1, 1, 1), \\ \hat{\mathcal{G}}^{(M_y)} &= \mathrm{diag}(-1, 1, -1, 1, 1, 1, 1, 1), \\ \hat{\mathcal{G}}^{(M_z)} &= \mathrm{diag}(1, 1, 1, 1, 1, 1, -1, -1), \end{aligned} \tag{3.5}$$

that compensates for the sign change in the hopping amplitudes between bonds. The gauge-dressed mirror operators are then defined as

$$\hat{M}_\alpha := \hat{\mathcal{G}}^{(M_\alpha)} \hat{M}_\alpha^0, \tag{3.6}$$

satisfying the symmetry condition $[\hat{M}_\alpha, \hat{H}_0] = 0$.

3.2.2 π-rotation symmetries

In this subsection, we examine the action of the three π-rotation operations around the x, y, and z axes. Rotations of π around the axis α act on the eight-dimensional single-particle Hilbert space effectively flipping the cubic cell along the two perpendicular directions, therefore acting as compositions of reflections. In particular, a π rotation around a given axis corresponds to a product of the two mirror operations across the planes perpendicular to that axis. In matrix representation, the action of bare π-rotation operations is expressed as

$$\begin{aligned}\hat{C}^0_{2,x} &= \hat{M}^0_y\,\hat{M}^0_z = \sigma^0 \otimes \sigma^x \otimes \sigma^x,\\ \hat{C}^0_{2,y} &= \hat{M}^0_x\,\hat{M}^0_z = \sigma^x \otimes \sigma^0 \otimes \sigma^x,\\ \hat{C}^0_{2,z} &= \hat{M}^0_x\,\hat{M}^0_y = \sigma^x \otimes \sigma^x \otimes \sigma^0.\end{aligned} \tag{3.7}$$

As for mirror operations, the presence of π-flux implies that the single-particle Hamiltonian is not conserved under these transformations, rotations altering the gauge structure of the hopping terms:

$$[\hat{C}^0_{2,\alpha}, \hat{H}_0] \neq 0, \quad \alpha = x, y, z. \tag{3.8}$$

We thus consider an appropriate gauge transformation for each operation:

$$\begin{aligned}\hat{\mathcal{G}}^{(C_{2,x})} &= \mathrm{diag}(-1, 1, -1, 1, -1, -1, 1, 1),\\ \hat{\mathcal{G}}^{(C_{2,y})} &= \mathrm{diag}(-1, 1, 1, 1, -1, 1, -1, -1),\\ \hat{\mathcal{G}}^{(C_{2,z})} &= \mathrm{diag}(1, -1, 1, 1, -1, -1, -1, 1),\end{aligned} \tag{3.9}$$

so that under each gauge-dressed rotation operator

$$\hat{C}_{2,\alpha} \coloneqq \hat{\mathcal{G}}^{(C_{2,\alpha})}\hat{C}^0_{2,\alpha}\,, \tag{3.10}$$

the single-particle Hamiltonian is invariant:

$$[\hat{C}_{2,\alpha}, \hat{H}_0] = 0. \tag{3.11}$$

It is worth noting that even under gauge transformations, rotational symmetries are combinations of gauge-dressed mirror symmetries:

$$\begin{aligned}\hat{C}_{2,x} &= \hat{M}_y\,\hat{M}_z,\\ \hat{C}_{2,y} &= \hat{M}_x\,\hat{M}_z,\\ \hat{C}_{2,z} &= \hat{M}_x\,\hat{M}_y.\end{aligned} \tag{3.12}$$

3.2.3 Inversion symmetry

The last transformation we consider is the inversion symmetry with respect to the center of the cube, $\mathcal{I}^0$, which is obtained as composition of all three mirror symmetries:

$$\hat{\mathcal{I}}^0 = \hat{M}_x^0\, \hat{M}_y^0\, \hat{M}_z^0, \tag{3.13}$$

Also in this case, the bare inversion transformation acts by altering the hopping pattern, implying $[\hat{\mathcal{I}}^0, \hat{H}_0] \neq 0$. The gauge transformation

$$\mathcal{G}^{(\mathcal{I})} = \mathrm{diag}(-1, 1, 1, 1, -1, -1, -1, 1), \tag{3.14}$$

allows us to define the dressed inversion operator

$$\hat{\mathcal{I}} = \mathcal{G}^{(\mathcal{I})} \hat{\mathcal{I}}^0 = \hat{M}_x\, \hat{M}_y\, \hat{M}_z, \tag{3.15}$$

which commutes with the single particle Hamiltonian, $[\hat{\mathcal{I}}, \hat{H}_0] = 0$, and thus represents a symmetry. Moreover, it is related to mirror and rotation operations by $\hat{C}_{2,\alpha}\, \hat{\mathcal{I}} = -\hat{M}_\alpha$.

3.2.4 Algebra of crystalline symmetries

Having introduced the reflection, inversion, and π-rotation symmetries of the cubic cell, we now examine the algebraic structure formed by these operations.

In the absence of the synthetic flux, symmetries of the system would be described by the commuting bare operators:

$$\begin{aligned}
[\hat{M}_\alpha^0, \hat{M}_\beta^0] &= 0, \\
[\hat{C}_{2,\alpha}^0, \hat{C}_{2,\beta}^0] &= 0, \\
[\hat{M}_\alpha^0, \hat{C}_{2,\beta}^0] &= 0,
\end{aligned} \tag{3.16}$$

and as a consequence, also the bare inversion transformation commutes with all the other symmetries.

In the presence of a π-flux, the gauge dressing required to restore Hamiltonian invariance modifies the standard commutation relations between spatial transformations, leading to a non-Abelian nature of the crystalline symmetry algebra [43]. In particular, the set of gauge-dressed mirror and π-rotation transformations forms a closed non-trivial algebra:

$$\begin{aligned}
[\hat{M}_\alpha, \hat{M}_\beta] &= 2\varepsilon_{\alpha\beta\gamma}\hat{C}_{2,\gamma} = 2\hat{M}_\alpha \hat{M}_\beta, \\
[\hat{C}_{2,\alpha}, \hat{C}_{2,\beta}] &= -2\varepsilon_{\alpha\beta\gamma}\hat{C}_{2,\gamma} = -2\hat{M}_\alpha \hat{M}_\beta, \\
[\hat{M}_\alpha, \hat{C}_{2,\beta}] &= -2\varepsilon_{\alpha\beta\gamma}\hat{M}_\gamma,
\end{aligned} \tag{3.17}$$

while they satisfy

$$\begin{aligned}\{\hat{M}_\alpha, \hat{M}_\beta\} &= 2\delta_{\alpha,\beta}\hat{\mathbb{1}},\\ \{\hat{C}_{2,\alpha}, \hat{C}_{2,\beta}\} &= -2\delta_{\alpha\beta}\hat{\mathbb{1}},\\ \{\hat{M}_\alpha, \hat{C}_{2,\beta}\} &= 2\delta_{\alpha,\beta}\hat{\mathcal{I}}.\end{aligned} \tag{3.18}$$

Regarding the inversion operation, this still commutes with all other symmetry transformations,

$$[\hat{\mathcal{I}}, \hat{M}_\alpha] = [\hat{\mathcal{I}}, \hat{C}_{2,\alpha}] = 0 \qquad \forall\, \alpha = x, y, z, \tag{3.19}$$

while the anticommutation relations are such that

$$\begin{aligned}\{\hat{M}_\alpha, \hat{\mathcal{I}}\} &= 2\hat{C}_{2,\alpha},\\ \{\hat{\mathcal{I}}, \hat{C}_{2,\alpha}\} &= 2\hat{M}_\alpha.\end{aligned} \tag{3.20}$$

One of the main effects of the π-flux geometric frustration is to induce a non-Abelian closed algebra among the crystalline symmetries of the cubic system. This is a direct consequence of the presence of the synthetic flux, and it is worth to bear it in mind for the implications it may have on the effective theory developed in the following Section. In particular, understanding how this closed algebra of cubic crystalline symmetries manifests in the low-energy projected theory can provide insight for an interpretation of interactions in a physically meaningful framework.

3.3 Effective theory in a symmetry-adapted basis

The non-Abelian structure of the symmetry algebra implies that not all symmetry operations can be diagonalized simultaneously. In this Section, we construct a symmetry-adapted basis by selecting a maximal commuting subset of these dressed symmetry operators. From the commutation relations in Eq. (3.17), it is clear that such a subset is given by one mirror symmetry and one π-rotation about the same axis. Without loss of generality, we select the set $\{\hat{M}_z, \hat{C}_{2,z}\}$ to be simultaneously diagonalized with the single-particle Hamiltonian $\hat{H}_0$. The common symmetry-adapted basis is defined by (see Appendix B)

$$|c_i\rangle = \sum_j \mathcal{T}_{ij}^{-1} |b_j\rangle\,, \tag{3.21}$$

where $|b_j\rangle = \hat{b}_j^\dagger |0\rangle$, with $j = 1, \ldots, 8$, are the basis states of the eight-dimensional Hilbert space of a single particle localized at site j of the cubic unit cell, while the

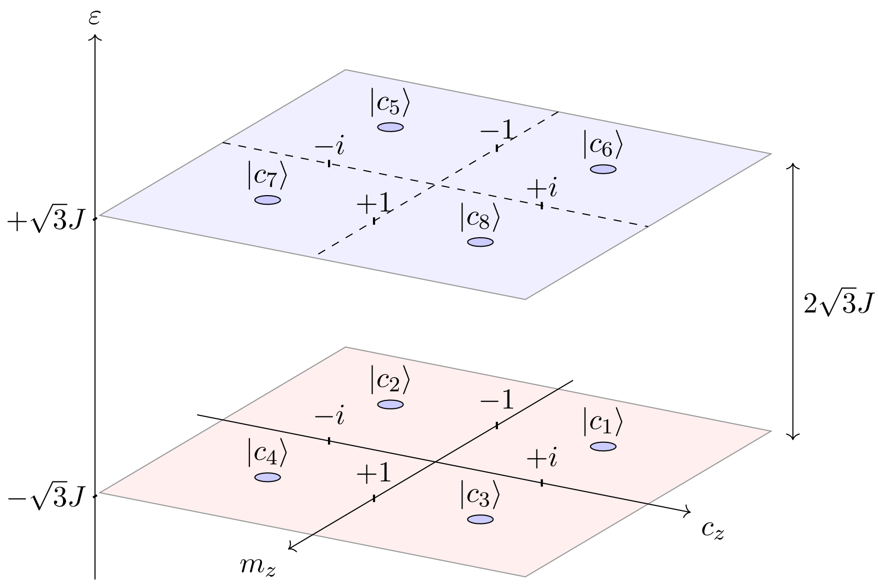

Figure 3.3: Three-dimensional representation of the symmetry-adapted single-particle eigenstates. Each group of four states lies on a plane corresponding to the energy eigenvalue $\varepsilon_\pm = \pm\sqrt{3}J$. The (m_z, c_z) quantum numbers span the in-plane structure.

single-particle states $|c_i\rangle$ denote the state of one boson occupying the orbital i, and $\mathcal{T}$ is the unitary matrix performing the change of basis. The explicit form of the matrix $\mathcal{T}$, together with details of the diagonalization procedure, is reported in Appendix B. Bosonic operators corresponding to symmetry eigenmodes are thus defined through the unitary transformation

$$\hat{b}_i = \sum_j \mathcal{T}_{ij}\hat{c}_j. \tag{3.22}$$

Each eigenstate $|c_i\rangle$ in this basis is labeled by a triplet of quantum numbers $(\varepsilon_i, m_z, c_z)$, corresponding to the energy, mirror parity, and rotation eigenvalue:

$$\hat{H}_0 |c_i\rangle = \varepsilon_i |c_i\rangle\,, \quad \hat{M}_z |c_i\rangle = m_z^{(i)} |c_i\rangle\,, \quad \hat{C}_{2,z} |c_i\rangle = c_z^{(i)} |c_i\rangle\,. \tag{3.23}$$

A visual representation of the energy levels and associated symmetry quantum numbers is shown in Fig. 3.3, which highlights the symmetry resolved organization of the single-particle eigenstates living in the two energy sectors sketched in Fig. 3.2.

Upon defining the projector operator $\hat{\mathcal{P}}$ onto the four-dimensional ground-state manifold spanned by the states $\{|c_1\rangle, |c_2\rangle, |c_3\rangle, |c_4\rangle\}$, the low-energy effective Hamiltonian can be written as:

$$\hat{H}^{\text{eff}} = \hat{\mathcal{P}}\hat{H}\hat{\mathcal{P}} = \hat{H}_0^{\text{eff}} + \hat{H}_{\text{int}}^{\text{eff}}. \tag{3.24}$$

The single-particle effective Hamiltonian reads

$$\hat{H}_0^{\text{eff}} = -\sqrt{3}J(\hat{c}_1^\dagger\hat{c}_1 + \hat{c}_2^\dagger\hat{c}_2 + \hat{c}_3^\dagger\hat{c}_3 + \hat{c}_4^\dagger\hat{c}_4) = -\sqrt{3}J\,\hat{N}, \tag{3.25}$$

with $\hat{N} = \sum_i \hat{c}_i^\dagger\hat{c}_i$ the total number of bosons, while the interacting part reads

$$\begin{aligned}\hat{H}_{\text{int}}^{\text{eff}} =& \frac{U}{12}(\hat{N}^2 - \hat{N}) + \frac{U}{6}(\hat{n}_1\hat{n}_2 + \hat{n}_3\hat{n}_4) \\ &- \sqrt{3}\frac{U}{24}\hat{c}_1^\dagger\hat{c}_1^\dagger\hat{c}_2\hat{c}_2 + \sqrt{3}\frac{U}{24}\hat{c}_3^\dagger\hat{c}_3^\dagger\hat{c}_4\hat{c}_4 \\ &+ \frac{U}{24}(\hat{c}_1^\dagger\hat{c}_1^\dagger\hat{c}_3\hat{c}_3 + \hat{c}_2^\dagger\hat{c}_2^\dagger\hat{c}_4\hat{c}_4) \\ &+ \frac{U}{6}(\hat{c}_1^\dagger\hat{c}_2^\dagger\hat{c}_3\hat{c}_4 + \hat{c}_1^\dagger\hat{c}_4^\dagger\hat{c}_3\hat{c}_2) + \text{H.c.}\ .\end{aligned} \tag{3.26}$$

The effective Hamiltonian $\hat{H}^{\text{eff}}$ in Eq. (3.24) describes a four-mode interacting bosonic system, where each orbital $\hat{c}_i$ belongs to a distinct symmetry sector of the projected model.

Interaction terms in $\hat{H}_{\text{int}}^{\text{eff}}$ can be classified according to the type of process they describe between these symmetry-labeled orbitals, and their action can be interpreted in terms of change or conservation of the associated crystalline quantum numbers.

Hubbard (local) terms

Terms of the form $\hat{c}_i^\dagger\hat{c}_i^\dagger\hat{c}_i\hat{c}_i$ describe on-site interactions between two bosons occupying the same orbital $\hat{c}_i$. These terms do not induce any change in the symmetry labels of the particles, and thus preserve both mirror and rotation eigenvalues. They appear in the first line of Eq. (3.26) with positive coefficients and energetically penalize configurations with multiple bosons in the same orbital. These interactions are local in orbital space, in the sense that they act within a single symmetry-labeled state. They appear for all four orbitals with equal weight, independently of the specific symmetry sector, and thus do not break the degeneracy among them.

Density-density interactions

Terms like $\hat{n}_i\hat{n}_j$ describe repulsive interactions between bosons occupying different orbitals, coupling the densities of different crystalline eigenstates without inducing transitions between them, leaving the symmetry configuration invariant. Their effect is to shift the energy of different configurations depending on the orbital occupations without inducing orbital mixing, acting as static constraints in the many-body Hilbert space. From Eq. (3.26), we observe that the dominant density-density interactions occur between orbitals that share the same mirror eigenvalue m_z. In particular, the terms $\hat{n}_1\hat{n}_2$ and $\hat{n}_3\hat{n}_4$ contribute to the energy cost associated with simultaneous occupation of the two orbitals within the same m_z-sector, thus favoring configurations where bosons are distributed across different sectors. As a consequence, density-density terms tend to suppress symmetry along m_z and promote a more balanced occupation among orbitals.

Orbital-changing terms

Pair-hopping terms of the form $\hat{c}_i^\dagger\hat{c}_i^\dagger\hat{c}_j\hat{c}_j$ describe orbital-changing collisions inducing correlated transfer of two bosons between orbitals with specific symmetry relations. Fig. 3.4 provides a schematic visualization of their action within the (m_z, c_z) symmetry sectors.

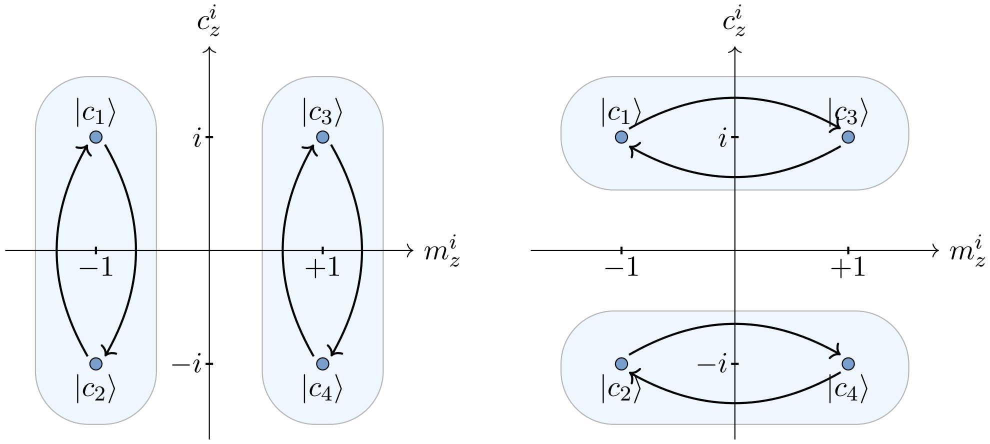

Figure 3.4: Graphical representation of orbital-changing interactions in the (m_z^i, c_z^i) plane. Left: intra-m_z sector processes, with opposite amplitude $\sqrt{3}\frac{U}{24}m_z$, couple orbitals with equal mirror eigenvalue m_z and opposite rotation eigenvalue c_z. Right: intra-c_z sector processes, with positive amplitude $\frac{U}{24}$, involve orbitals with the same c_z but opposite m_z eigenvalue. Arrows represent correlated two-boson transfer between orbitals induced by pair-hopping terms.

We distinguish two kinds of orbital-changing terms depending on the symmetry quantum numbers they relate to:

- **Intra-m_z sector interactions**:
  Terms such as $\hat{c}_1^\dagger\hat{c}_1^\dagger\hat{c}_2\hat{c}_2$ and $\hat{c}_3^\dagger\hat{c}_3^\dagger\hat{c}_4\hat{c}_4$ couple orbitals that share the same mirror eigenvalue m_z but have opposite rotation eigenvalue c_z. These

are the dominant pair-hopping contributions, as indicated by the larger prefactors in Eq. (3.26), with an attractive and repulsive sign, respectively.

- **Intra-c_z sector interactions**:
  The terms $\hat{c}_1^\dagger\hat{c}_1^\dagger\hat{c}_3\hat{c}_3$ and $\hat{c}_2^\dagger\hat{c}_2^\dagger\hat{c}_4\hat{c}_4$ instead connect orbitals with the same c_z eigenvalue but opposite mirror eigenvalue m_z, and appear in Eq. (3.26) with a positive and smaller prefactor with respect to the ones acting on intra-m_z sectors.

Mixing terms

Orbital-mixing terms of the form $\hat{c}_i^\dagger\hat{c}_j^\dagger\hat{c}_k\hat{c}_l$, with $i \neq j \neq k \neq l$, involve all four orbitals and describe exchange processes between pairs of bosons belonging to different symmetry sectors. A graphical interpretation of their action in the (m_z, c_z) plane is provided in Fig. 3.5.

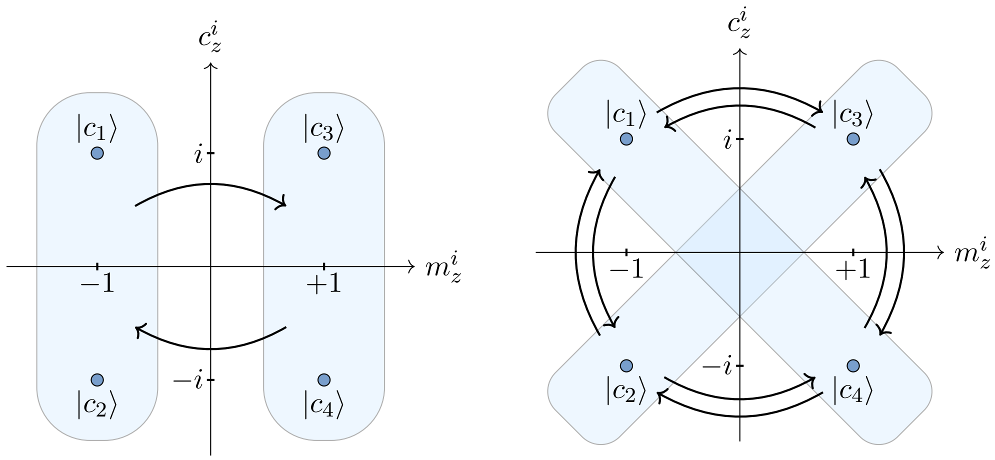

Figure 3.5: Graphical representation of orbital mixing terms in the (m_z^i, c_z^i) plane. Left: inter-m_z processes transfer pairs of bosons between mirror sectors while preserving their rotation eigenvalues. Right: cross-sector processes correspond to a simultaneous exchange of both m_z and c_z components, effectively rotating the boson configuration across sectors while preserving the total crystalline quantum numbers. Both processes appear with a positive amplitude equal to $\frac{U}{6}$.

We identify two types of orbital-mixing interaction, appearing in the interacting Hamiltonian (3.26) with the same positive amplitude:

- **Inter-m_z process**:
  The terms $\hat{c}_1^\dagger\hat{c}_2^\dagger\hat{c}_3\hat{c}_4$ transfer two particles with opposite c_z from the $m_z = -1$ orbitals to the $m_z = +1$ orbitals, still with opposite c_z, and vice versa. These processes can be interpreted as a transfer of boson population across mirror sectors.

- **Cross-sector rotation**:
  The terms $\hat{c}_1^\dagger \hat{c}_4^\dagger \hat{c}_2 \hat{c}_3$ do not act within a single symmetry sector. They annihilate a pair of bosons in the states $(m_z, c_z) = (-1, -i)$ and $(+1, +i)$, and creates a pair in $(+1, -i)$ and $(-1, +i)$, and vice versa, preserving the global configuration of crystalline quantum numbers. These transformations can be viewed as $\pi/2$ rotations of the distribution of eigenvalue pairs in the (m_z, c_z) plane while keeping their sum unchanged. The global symmetry content is preserved, but the processes connect configurations with different local symmetry labels.

Missing terms

Some interaction terms that would be compatible with the crystalline symmetries of the system do not appear in the effective Hamiltonian in Eq. (B.12). In particular, we notice the absence of pair-hopping processes between orbitals $(1, 4)$ and $(2, 3)$, described by orbital-changing terms of the form $\hat{c}_1^\dagger \hat{c}_1^\dagger \hat{c}_4 \hat{c}_4$ and $\hat{c}_2^\dagger \hat{c}_2^\dagger \hat{c}_3 \hat{c}_3$. These processes would correspond to a simultaneous change in the sign of all quantum numbers, with the only conservation of the total sum.

Similarly, quartic terms $\hat{c}_1^\dagger \hat{c}_3^\dagger \hat{c}_2 \hat{c}_4$ are also not present. These terms would transfer two particles with opposite m_z from the $c_z = -i$ sector to the $c_z = +i$ one, keeping opposite m_z, and vice versa. In our notation, they would be denoted as inter-c_z sector interactions and could be interpreted as a transfer of boson population across rotation sectors. Their absence suggests that simultaneous changes of the c_z quantum number in both particles are not allowed by the structure of the interaction.

The absence of these terms may reflect additional constraints beyond symmetry, possibly arising from the structure of the projected interactions.

Emergent symmetries in the effective Hamiltonian

Beyond the crystalline symmetries inherited from the underlying cubic geometry, the effective Hamiltonian $\hat{H}_{\text{eff}}$ exhibits two additional emergent symmetries, which act on the orbital degrees of freedom $\{\hat{c}_1, \hat{c}_2, \hat{c}_3, \hat{c}_4\}$ permuting the orbitals in a way that preserves both the total energy and the symmetry structure of the interaction terms:

$$\begin{aligned} \hat{T}_\alpha : \quad & \hat{c}_1 \to \hat{c}_2, \qquad \hat{c}_2 \to \hat{c}_1, \\ & \hat{c}_3 \to \hat{c}_4, \qquad \hat{c}_4 \to \hat{c}_3, \end{aligned} \tag{3.27}$$

$$\begin{aligned} \hat{T}_\beta : \quad & \hat{c}_1 \to \hat{c}_3 \qquad \hat{c}_2 \to i\hat{c}_4, \\ & \hat{c}_3 \to \hat{c}_1, \qquad \hat{c}_4 \to i\hat{c}_2. \end{aligned} \tag{3.28}$$

These transformations leave the effective Hamiltonian invariant, which is equivalent to saying that they commute with it:

$$[\hat{T}_\alpha, \hat{H}_{\text{eff}}] = [\hat{T}_\beta, \hat{H}_{\text{eff}}] = 0. \tag{3.29}$$

In the four-dimensional single-particle subspace spanned by the low-energy modes, they are represented by the matrices

$$\hat{T}_\alpha = \begin{pmatrix} 0 & 1 & 0 & 0 \\ 1 & 0 & 0 & 0 \\ 0 & 0 & 0 & 1 \\ 0 & 0 & 1 & 0 \end{pmatrix}, \qquad \hat{T}_\beta = \begin{pmatrix} 0 & 0 & 1 & 0 \\ 0 & 0 & 0 & i \\ 1 & 0 & 0 & 0 \\ 0 & i & 0 & 0 \end{pmatrix}. \tag{3.30}$$

These operations reflect an internal symmetry of the orbital manifold induced by the structure of the projected interactions and provide a basis for a systematic investigation of the hidden symmetries in the effective theory. It would be of interest to investigate whether and how these emergent symmetries are connected to the crystalline transformations in the full eight-dimensional space, forming the closed non-Abelian algebra discussed in the previous Section.

3.4 Algebraic structure and spectrum generating algebra

Having analyzed the structure of the effective Hamiltonian and identified its emergent symmetries, we now aim to develop an algebraic description of the four-orbital model. The goal is to identify a hidden Lie algebra and reformulate the effective theory in terms of a so-called *dynamical symmetry* (also *spectrum generating algebra*) [52, 53]: a formulation in which the operators governing the dynamics form a closed algebra and the Hamiltonian can be written in terms of its generators and Casimir operators. This approach provides a compact representation of the interactions and enables a systematic classification of eigenstates in terms of the associated Casimir eigenvalue.

In the two-dimensional case, such a representation is obtained by constructing bilinear operators from the generators of the Lie algebra of $SU(2)$. In the same spirit, an algebraic representation of $\hat{H}_{\text{eff}}$ can be achieved by generalizing the Schwinger bosons construction: bilinear operators are built from the four bosonic modes $\hat{c}_i$ by using generators of a larger Lie algebra with four-dimensional matrix representation.

The starting point is the general structure of the effective Hamiltonian (3.24), which involves quadratic and quartic interaction terms among the four orbital modes:

$$\hat{H}_{\text{eff}} = \sum_{ij} h_{ij}\, \hat{c}_i^\dagger \hat{c}_j + \sum_{ijkl} U_{ijkl}\, \hat{c}_i^\dagger \hat{c}_j \hat{c}_k^\dagger \hat{c}_l, \tag{3.31}$$

where $h = h^\dagger$ is a 4×4 Hermitian matrix, while U is a rank-4 Hermitian tensor satisfying $U_{ijkl} = U^*_{klij}$.

Given a complete set $\{\Gamma^\mu\}$ of Hermitian matrices acting on $\mathbb{C}^4$, the general strategy is to define bilinear operators as

$$\hat{B}_\mu = \sum_{\alpha\beta} \hat{c}_\alpha^\dagger \Gamma^\mu_{\alpha\beta} \hat{c}_\beta, \tag{3.32}$$

and to rewrite the effective Hamiltonian (3.31) as a sum of linear and bilinear terms in these operators:

$$\hat{H}_{\text{eff}} = \sum_{\mu} f_\mu \hat{B}_\mu + \sum_{\mu\nu} f_{\mu\nu} \hat{B}_\mu \hat{B}_\nu\,. \tag{3.33}$$

3.4.1 Basis of Hermitian matrices

As a first step, we consider the set of 16 matrices $\{\Gamma^\mu\}_{\mu=1}^{16}$ constructed from Dirac matrices and their products, which form a complete basis for the space $\mathbb{C}^4$ of 4×4 Hermitian matrices [54, 55]. To ensure hermiticity and normalization with respect to the Hilbert-Schmidt inner product

$$\mathrm{Tr}\left[(\Gamma^\mu)^\dagger \Gamma^\nu\right] = \delta^{\mu\nu}, \tag{3.34}$$

we take the set

$$\begin{aligned}
\Gamma^\mu = \Big\{ &\frac{1}{2}\gamma_0, \quad \frac{i}{2}\gamma_1, \quad -\frac{i}{2}\gamma_2, \quad \frac{i}{2}\gamma_3, \\
&\quad \gamma_5 = \frac{i}{2}\gamma_0\gamma_1\gamma_2\gamma_3, \\
&\frac{i}{2}\gamma_0\gamma_5, \quad \frac{1}{2}\gamma_1\gamma_5, \quad -\frac{1}{2}\gamma_2\gamma_5, \quad \frac{1}{2}\gamma_3\gamma_5, \\
&-\frac{i}{2}\sigma^{01}, \quad \frac{i}{2}\sigma^{02}, \quad \frac{i}{2}\sigma^{03}, \quad \frac{1}{2}\sigma^{12}, \quad -\frac{1}{2}\sigma^{13}, \quad \frac{1}{2}\sigma^{23}, \\
&\frac{1}{2}\mathbb{1}\Big\},
\end{aligned} \tag{3.35}$$

where the spin matrices are defined as

$$\sigma^{\mu\nu} = \frac{i}{2}[\gamma^\mu, \gamma^\nu], \tag{3.36}$$

and Dirac matrices are considered in Dirac representation

$$\gamma^0 = \begin{pmatrix} \sigma^0 & 0 \\ 0 & -\sigma^0 \end{pmatrix}, \quad \gamma^k = \begin{pmatrix} 0 & \sigma^k \\ -\sigma^k & 0 \end{pmatrix}, \quad \gamma^5 = \begin{pmatrix} 0 & \sigma^0 \\ \sigma^0 & 0 \end{pmatrix}, \tag{3.37}$$

in terms of the Pauli matrices σ^k and the 2×2 identity matrix σ^0.

3.4.2 Expansion in Γ matrices

The correspondence with the expansion in (3.33) is obtained by expanding the matrix h and the tensor U in terms of the basis set (3.35). For the bilinear term this means

$$h = \sum_\mu f_\mu \Gamma^\mu, \tag{3.38}$$

so that

$$\sum_{ij} h_{ij} \hat{c}_i^\dagger \hat{c}_j = \sum_\mu \sum_{ij} f_\mu \hat{c}_i^\dagger \Gamma_{ij}^{(\mu)} \hat{c}_j\,, \tag{3.39}$$

where the Hermitian condition $(\Gamma^{(\mu)})^\dagger = \Gamma^{(\mu)}$ implies

$$f_\mu = f_\mu^* \implies f_\mu \in \mathbb{R}\,. \tag{3.40}$$

In particular, in order to reproduce the effective Hamiltonian (3.25), the hopping matrix has to be proportional to the 4×4 identity matrix:

$$h = -\sqrt{3} J\, \mathbb{1}\,, \tag{3.41}$$

thus the bilinear terms are simply

$$\sum_{ij} h_{ij}\, \hat{c}_i^\dagger \hat{c}_j = \sum_{ij} (-2\sqrt{3}J)\, \hat{c}_i^\dagger \Gamma_{ij}^{16} \hat{c}_j = -\sqrt{3} J\, \hat{N} \tag{3.42}$$

with a unique coefficient in the expansion $f_{16} = -2\sqrt{3}J$.

Regarding the quartic term, the elements of the Hermitian tensor U_{ijkl} can be viewed as the components of an operator U acting on the tensor product space $\mathbb{C}^4 \otimes \mathbb{C}^4$. The operator can then be expanded using tensor operator expansion over the product basis $\{\Gamma^\mu \otimes \Gamma^\nu\}_{\mu,\nu=1}^{16}$ of 16×16 matrices as

$$U = \sum_{\mu,\nu=1}^{16} f_{\mu\nu}\, \Gamma^\mu \otimes \Gamma^\nu, \tag{3.43}$$

so that the tensor components read

$$U_{ijkl} = \sum_{\mu,\nu=1}^{16} f_{\mu\nu}\, \Gamma^{\mu}_{ij} \otimes \Gamma^{\nu}_{kl}, \tag{3.44}$$

with $f_{\mu\nu} \in \mathbb{C}$, and the Hermitian condition implies

$$U = U^{\dagger} \implies f_{\mu\nu} = f^{*}_{\nu\mu}. \tag{3.45}$$

The decomposition in (3.43) is essentially a Hilbert-Schmidt expansion of an operator on a composite Hilbert space (operator basis expansion in tensor product spaces): if $\{\Gamma^{\mu}\}$ is an orthonormal basis for Hermitian operators on $\mathbb{C}^n$ with respect to the Hilbert-Schmidt inner product, then any Hermitian operator $U \in \mathbf{Herm}(\mathbb{C}^n \otimes \mathbb{C}^n)$ can be written as:

$$U = \sum_{\mu,\nu} \mathrm{Tr}[(\Gamma^{\mu} \otimes \Gamma^{\nu})^{\dagger} U]\, \Gamma^{\mu} \otimes \Gamma^{\nu}. \tag{3.46}$$

This decomposition provides a complete and orthogonal basis for expressing arbitrary quartic interaction terms. The coefficients $f_{\mu\nu}$ encode the full structure of two-body processes in terms of symmetry-adapted bilinears, and allow us to reorganize $\hat{H}_{\text{eff}}$ in terms of algebraic structured interaction terms.

We extract the coefficients $f_{\mu\nu}$ by projecting the operator U onto the basis (3.35), using the Hilbert-Schmidt inner product:

$$f_{\mu\nu} = \mathrm{Tr}\left[(\Gamma^{\mu} \otimes \Gamma^{\nu})^{\dagger} U\right], \tag{3.47}$$

so that expansion (3.33) of the effective Hamiltonian in terms of the Γ-bilinear operators reads

$$\begin{aligned}\hat{H}_{\text{eff}} = &-\Big(\sqrt{3}J + \frac{U}{12}\Big)\hat{N} + \frac{5U}{12}\hat{B}_{16}^2 + \frac{U}{8}\hat{B}_5^2 + \frac{U}{12}\left(\hat{B}_1^2 - \hat{B}_9^2 - \hat{B}_{13}^2\right) \\ &- \frac{U}{8\sqrt{3}}\left(\hat{B}_7\hat{B}_{15} + \hat{B}_{15}\hat{B}_7 + \hat{B}_8\hat{B}_{14} + \hat{B}_{14}\hat{B}_8\right) \\ &- \frac{U}{24}\left(\hat{B}_2^2 + \hat{B}_3^2 + \hat{B}_4^2 + \hat{B}_6^2 + \hat{B}_7^2 + \hat{B}_8^2 + \hat{B}_{12}^2\right) \\ &+ \frac{U}{24}\left(\hat{B}_{10}^2 + \hat{B}_{11}^2 - \hat{B}_{14}^2 - \hat{B}_{15}^2\right).\end{aligned} \tag{3.48}$$

Decomposition (3.48) in terms of Γ-matrices provides a general and complete symmetry-compatible formulation in terms of bilinear operators. However, it does not reveal an underlying Lie algebraic structure or an associated symmetries of the effective Hamiltonian. We can gain further insight by applying the same general construction to the generators of a specific Lie algebra that reflects the symmetry content of the four-orbital model.

3.4.3 $\mathfrak{su}(4)$ representation

The developed method applies to any complete set of Hermitian generators of a symmetry group with a four-dimensional representation. In particular, it comes out that the four-mode effective Hamiltonian can be written in terms of bilinears constructed from the generators of the Lie algebra of $SU(4)$.

To show this, we adopt the same notation for the matrix representation of $\mathfrak{su}(4)$ presented in [56], and define the corresponding bilinear operators as:

$$\hat{\lambda}_\mu = \sum_{\alpha\beta} \hat{c}^\dagger_\alpha \Lambda^{\alpha\beta}_\mu \hat{c}_\beta, \tag{3.49}$$

where $\{\Lambda_\mu\}_{\mu=1}^{15}$ denotes the 15 traceless Hermitian generators of $\mathfrak{su}(4)$, and Λ_{16} is the 4×4 identity matrix completing the basis. In terms of $SU(4)$ bilinears, the effective Hamiltonian (3.31) reads

$$\begin{aligned}\hat{H}_{\text{eff}} = &-\Big(\sqrt{3}J + \frac{U}{12}\Big)\hat{N} + \frac{5U}{12}\hat{N}^2 - \frac{U}{12}\hat{\lambda}_3^2 + \frac{U}{36}\Big(\hat{\lambda}_8^2 - \hat{\lambda}_{15}^2\Big) \\ &+ \frac{U}{8\sqrt{3}}\Big(-\hat{\lambda}_1^2 + \hat{\lambda}_2^2 + \hat{\lambda}_{13}^2 - \hat{\lambda}_{14}^2\Big) + \frac{U}{24}\Big(\hat{\lambda}_4^2 - \hat{\lambda}_5^2 + \hat{\lambda}_{11}^2 - \hat{\lambda}_{12}^2\Big) \\ &+\frac{U}{24}\Big(\hat{\lambda}_1\hat{\lambda}_{13} + \hat{\lambda}_{13}\hat{\lambda}_1 + \hat{\lambda}_2\hat{\lambda}_{14} + \hat{\lambda}_{14}\hat{\lambda}_2 + \hat{\lambda}_6\hat{\lambda}_9 + \hat{\lambda}_9\hat{\lambda}_6 - \hat{\lambda}_7\hat{\lambda}_{10} - \hat{\lambda}_{10}\hat{\lambda}_7\Big) \\ &+ \frac{U}{12}\Big(\hat{\lambda}_4\hat{\lambda}_{11} + \hat{\lambda}_{11}\hat{\lambda}_4\Big) + \frac{U}{9\sqrt{2}}\Big(\hat{\lambda}_8\hat{\lambda}_{15} + \hat{\lambda}_{15}\hat{\lambda}_8\Big)\,,\end{aligned} \tag{3.50}$$

where in the four-mode representation $\hat{\lambda}_{16} = \hat{N}$ is the total number operator.

Expansion in Eq. (3.50) points out a natural organization of the theory in terms of Schwinger-type bilinears built from generators of the Lie algebra $\mathfrak{su}(4)$, allowing us to rewrite both the quadratic and quartic terms of the effective Hamiltonian in a compact and symmetry-aware form. This reveals an underlying algebraic structure that leads to the identification of an emergent $SU(4)$ symmetry in the projected low-energy theory. However, while the purpose of this expansion was to investigate whether the effective Hamiltonian exhibits clear symmetry properties when expressed in terms of $SU(4)$ bilinears, in analogy with the $SU(2)$ representation of the two-dimensional case, no particularly simple algebraic structure emerges at this level, and thus no direct connection with the 2D case can be established. However, numerical results presented in the next Chapter reveal a systematic, although complex, organization of the spectra. This hints at a possible hidden structure for which the above construction might reveal useful.

4 Numerical Results

In this final Chapter, we present the results of the numerical analysis of the three-dimensional bosonic BBH model introduced and theoretically developed in the previous sections.

In the first Section, we validate our theoretical results by performing exact diagonalization (ED) of the full Bose-Hubbard Hamiltonian on the π-flux cube, and compare its energy spectrum with the one obtained from the projected theory. This comparison allows us to assess the accuracy of the effective model in capturing the correct low-energy physics, and to examine the structure and degeneracies of the energy levels.

In the second Section, we numerically investigate the properties of the classical ground state in the weakly interacting regime within a mean-field approach. Starting from the classical energy functional derived from the effective theory, we determine its global minima by combining a discrete Gross-Pitaevskii description with an imaginary time evolution (ITE) approach. We then apply the same framework to the full eight-mode model. For sufficiently weak interactions, the two descriptions are expected to yield equivalent results.

4.1 Exact diagonalization and comparison with the effective theory

In this Section, we expose the results of the calculation of the many-body energy spectrum of the full Bose–Hubbard Hamiltonian (3.1) on the π-flux cube, and discuss the comparison with the spectrum of the four-mode effective theory described by the projected Hamiltonian in Eq. (3.24). Both models are diagonalized using exact diagonalization via the Python package `QuSpin` [57]. The comparison, shown in Fig. 4.1 for several values of the boson number N, highlights

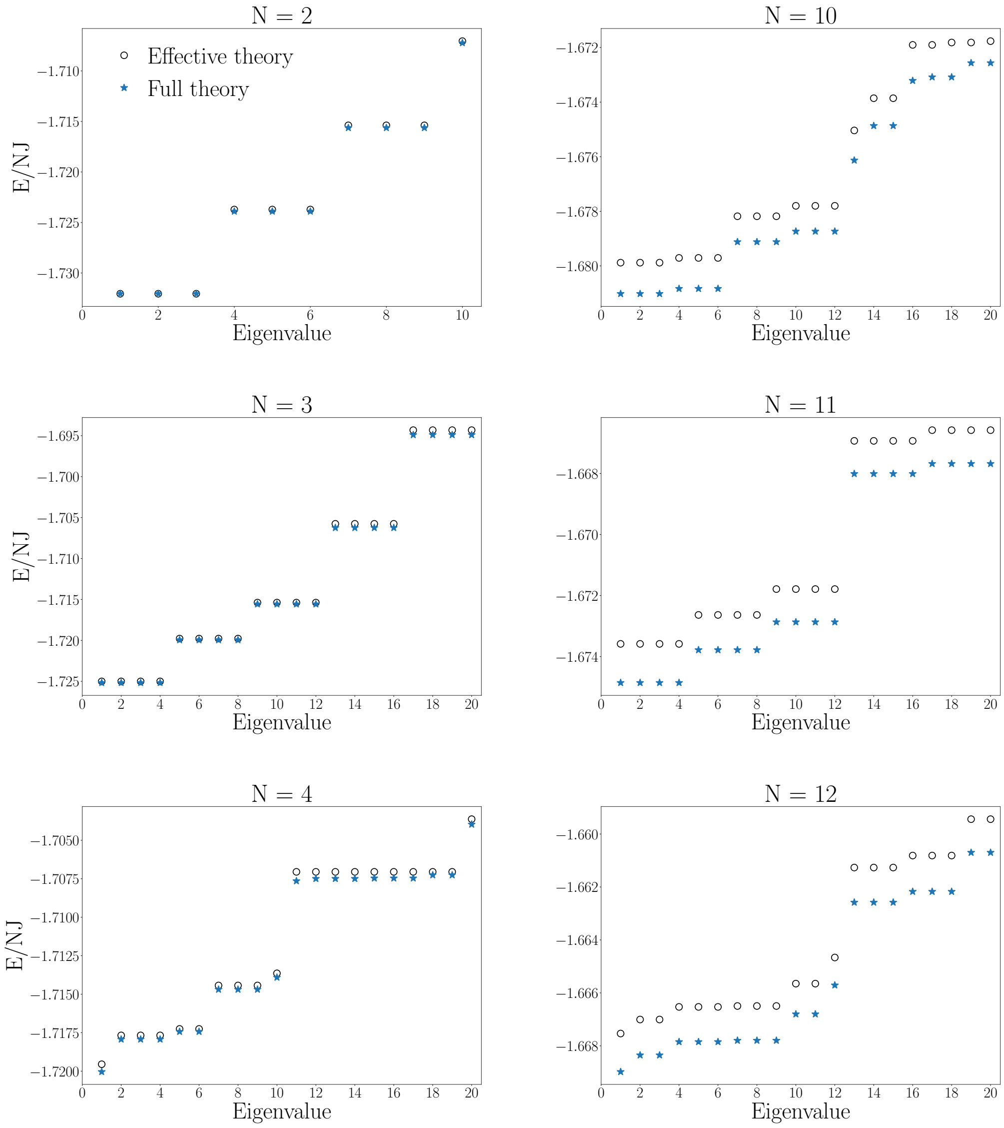

Figure 4.1: Comparison between the energy spectra of the effective and full theories for different boson numbers N at fixed $U = 0.1J$. The spectra are obtained by exact diagonalization.

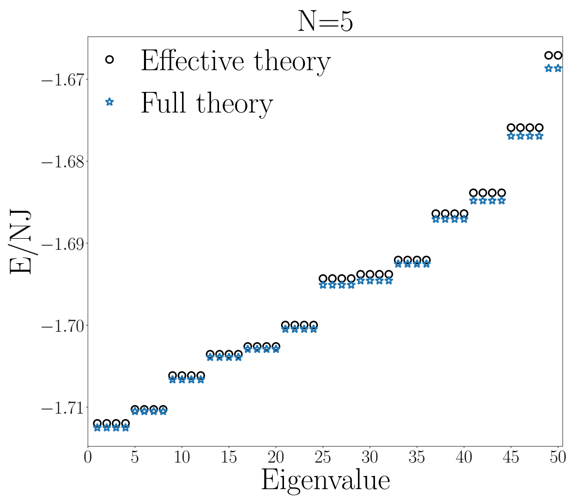

Figure 4.2: Energy spectrum for $N = 5$ and $U = 0.1J$. The fourfold degeneracy pattern is clearly visible and stable over many energy levels. The effective theory accurately reproduces the full spectrum.

the accuracy of the effective model in capturing the correct low-energy structure. In particular, we observe that the projected theory properly reproduces the distribution and degeneracy pattern of the energy levels, albeit uniform energy shift with respect to the full theory, which we analyze below.

A notable feature of the energy spectrum in Fig. 4.1 is its strong dependence on the filling $\nu = N/8$, which directly affects the degeneracy structure of the eigenstates. The addition of a single boson utterly alters the degeneracy pattern, leading to different spectral structures. This filling dependence in the spectrum reveals purely quantum effects arising from frustration and interactions, and is remarkably different from the two-dimensional single-plaquette case discussed in Chapter 2, where the degeneracy structure was independent of the filling and exhibited a simpler regular organization. In the cubic cell case, the resulting degeneracy structure exhibits distinct behavior depending on whether the number of bosons is odd, even, or a multiple of four:

- For an odd number of bosons, the spectrum displays a highly regular structure, with a four-fold degeneracy of the eigenstates stable across a broad number of excited states. This is clearly visible in Fig. 4.2, where the first 50 eigenvalues are shown for $N = 5$.
- For even N not divisible by 4, such as $N = 2, 6, 10, \ldots$, we observe a threefold degeneracy in the lowest levels.
- For N divisible by 4 (e.g., $N = 4, 8, 12, \ldots$), the ground state is non-degenerate. This indicates that the degeneracy-protecting symmetry is lifted at these fillings.

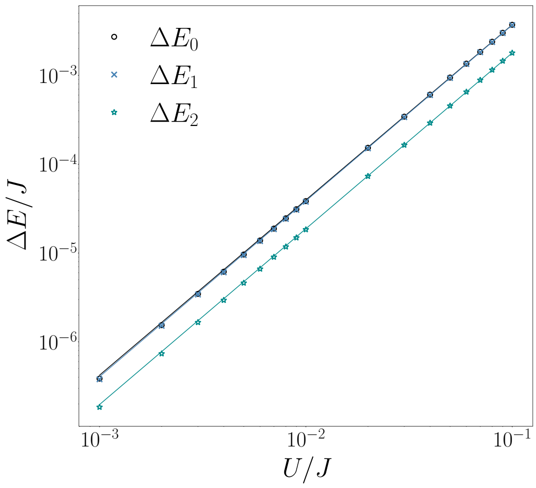

Figure 4.3: Plot in log-log scale of the energy differences $\Delta E_i = E_i^{\text{full}} - E_i^{\text{eff}}$ between the exact and effective spectra for $N = 6$ as a function of U. The linear fits $\Delta E_i \propto U^{\beta_i}$ confirm that the shifts scale as $\beta_i \simeq 2$, coherently with second-order perturbation theory.

The highly regular structure observed in the spectra, especially for odd N, suggests the presence of an underlying algebraic structure. This aligns with the $SU(4)$ formulation introduced earlier, which may serve as the basis for a full algebraic classification of the spectrum. We leave this analysis to future investigations.

To understand the energy shift between the two models, we compute the energy difference $\Delta E_i = E_i^{\text{full}} - E_i^{\text{eff}}$ for the i-th degenerate energy sector as a function of U, where $i = 0$ corresponds to the ground state manifold. This is illustrated in Fig. 4.3, where the energy difference between the two spectra is shown to scale quadratically with the interaction strength U, consistently with second-order perturbative corrections. In particular, linear fits in Fig. 4.3 result in the scaling exponents

$$\begin{aligned}
\beta_0 &= 1.972 \pm 0.001, \\
\beta_1 &= 1.979 \pm 0.001, \\
\beta_2 &= 1.979 \pm 0.001,
\end{aligned} \tag{4.1}$$

where errors correspond to one standard deviation obtained from the least-squares fit. The discrepancy ΔE can be attributed to the contribution of high-energy orbitals that are neglected in the projected theory, and which become increasingly relevant as the number of bosons grows. These corrections originate from virtual processes involving higher-energy modes, whose transition amplitude in perturbation theory is of the order of $U^2/\Delta\varepsilon$, with $\Delta\varepsilon = 2\sqrt{3}J$ being the single-particle gap.

4.2 Gross-Pitaevskii theory

Having established the validity of the effective theory in reproducing the correct low-energy physics, we now turn to a mean-field analysis of the classical ground-state structure, similarly to what we have done in Section 2.4 for the two-dimensional case. In the limit of weak interactions and large particle number, the system can be described within a mean-field Gross–Pitaevskii theory [58, 59]. Assuming complete condensation, the condensate wavefunction can be obtained by solving the variational problem for the average energy per particle. In this Section, we investigate the classical ground-state structure by minimizing the energy functional derived from both the effective four-mode theory and the full eight-mode Bose–Hubbard model.

4.2.1 Gross-Pitaevskii description of the effective theory

We develop a mean-field description of the low-energy theory by studying the classical energy functional resulting from the effective Hamiltonian in Eq. (3.24). In the thermodynamic limit $N \to \infty$ and for finite $g \equiv UN$, with $U \to 0$, we assume all bosons to condensate into the same coherent ground state and replace the bosonic operators $\hat{c}_i$ with the *ansatz* for their expectation values:

$$\hat{c}_\alpha \to c_\alpha \equiv \langle \hat{c}_\alpha \rangle = |c_\alpha|\, e^{i\theta_{c\alpha}}, \qquad \alpha = 1, \dots, 4, \tag{4.2}$$

such that in the condensate phase $\sum_\alpha |c_\alpha|^2 = N$, and global $U(1)$ symmetry allows to fix one of the phases $\theta_{c_\alpha} = 0$.

Substituting into Eq. (3.24), the resulting four-orbital classical energy functional takes the form

$$\begin{aligned}
E_{\mathrm{MF}}[\{c_\alpha, c_\alpha^*\}] = E(N) &+ \frac{U}{6}\left(|c_1|^2\,|c_2|^2 + |c_3|^2\,|c_4|^2\right) \\
&+ \frac{\sqrt{3}}{12}U\Big(- |c_1|^2\,|c_2|^2 \cos 2(\theta_{c_2} - \theta_{c_1}) + |c_3|^2\,|c_4|^2 \cos 2(\theta_{c_4} - \theta_{c_3})\Big) \\
&+ \frac{U}{12}\Big(|c_1|^2\,|c_3|^2 \cos 2(\theta_{c_3} - \theta_{c_1}) + |c_2|^2\,|c_4|^2 \cos 2(\theta_{c_4} - \theta_{c_2})\Big) \\
&+ 2\frac{U}{3}\,|c_1|\,|c_2|\,|c_3|\,|c_4| \cos(\theta_{c_3} - \theta_{c_1}) \cos(\theta_{c_2} - \theta_{c_4}),
\end{aligned} \tag{4.3}$$

with $E(N) = -\left(\sqrt{3}J + \frac{U}{12}\right) N$.

To determine the classical ground state, we have to look for the global minima of the energy functional $E_{\mathrm{MF}}[\{c_\alpha, c_\alpha^*\}]$ over the eight real parameters $\{|c_\alpha|, \theta_{c_\alpha}\}$, by solving the stationarity conditions

$$\frac{\partial E_{\mathrm{MF}}}{\partial |c_\alpha|} = 0, \qquad \frac{\partial E_{\mathrm{MF}}}{\partial \theta_{c_\alpha}} = 0, \qquad \forall \alpha = 1, \ldots, 4. \tag{4.4}$$

Remarkably, the energy landscape is characterized by a dense manifold of nearly degenerate low-energy states, signaling the presence of a complex classical phase structure. To systematically explore this landscape and identify the classical ground states, we employ a numerical method that combines a discrete Gross–Pitaevskii description with imaginary time evolution [60, 61].

Starting from the time-dependent Gross-Pitaevskii equation for the complex fields $\{c_\alpha\}$:

$$i\partial_t c_\alpha(t) = \frac{\delta E[c, c^*]}{\delta c_\alpha^*}, \tag{4.5}$$

with $E[c, c^*]$ being the energy functional in Eq. (4.3), we search for stationary solutions of the form

$$c_\alpha(t) = c_\alpha(0) e^{-i\mu t}, \tag{4.6}$$

where the time dependence is fixed by the chemical potential $\mu = \frac{\partial E}{\partial N}$. Substituting into Eq. (4.5), we reformulate the problem as a system of stationary Gross–Pitaevskii equations for the bosonic low-energy classical modes:

$$\mu c_\alpha = \frac{\delta E[c, c^*]}{\delta c_\alpha^*} \quad \text{for} \quad \alpha = 1, 2, 3, 4. \tag{4.7}$$

It is convenient to solve Eq. (4.7) after having renormalized the parameters $\{c_i\}$ with the total number of bosons

$$c_\alpha \to \sqrt{N} c_\alpha, \tag{4.8}$$

so that

$$\sum_\alpha |c_\alpha|^2 = 1, \tag{4.9}$$

and the Gross-Pitaevskii equations become dependent only on the effective coupling constant $g = UN$, and not explicitly on the number of bosons.

The Gross-Pitaevskii equations for the four fields explicitly read

$$\begin{aligned}\mu c_1 = &\left(-\sqrt{3}J + \frac{g}{3}|c_2|^2 + \frac{g}{6}(|c_1|^2 + |c_3|^2 + |c_4|^2)\right)c_1 - \sqrt{3}\frac{g}{12}(c_1^* c_2)c_2 + \frac{g}{12}(c_4^* c_3)c_2 \\ &+ \frac{g}{12}(c_1^* c_3)c_3 + \frac{g}{12}(c_4^* c_2)c_3 + \frac{g}{12}(c_2^* c_4)c_3 + \frac{g}{12}(c_2^* c_3)c_4,\end{aligned}$$

$$\mu c_2 = \Big(-\sqrt{3}J + \frac{g}{3}|c_1|^2 + \frac{g}{6}(|c_2|^2 + |c_3|^2 + |c_4|^2)\Big)c_2 - \sqrt{3}\frac{g}{12}(c_2^* c_1)c_1 + \frac{g}{12}(c_3^* c_4)c_1$$
$$+ \frac{g}{12}(c_1^* c_4)c_3 + \frac{g}{12}(c_2^* c_4)c_4 + \frac{g}{12}(c_1^* c_3)c_4 + \frac{g}{12}(c_3^* c_1)c_4, \quad (4.10)$$

$$\mu c_3 = \Big(-\sqrt{3}J + \frac{g}{3}|c_4|^2 + \frac{g}{6}(|c_3|^2 + |c_1|^2 + |c_2|^2)\Big)c_3 + \sqrt{3}\frac{g}{12}(c_3^* c_4)c_4 + \frac{g}{12}(c_2^* c_1)c_4$$
$$+ \frac{g}{12}(c_4^* c_1)c_2 + \frac{g}{12}(c_3^* c_1)c_1 + \frac{g}{12}(c_2^* c_4)c_1 + \frac{g}{12}(c_4^* c_2)c_1,$$

$$\mu c_4 = \Big(-\sqrt{3}J + \frac{g}{3}|c_3|^2 + \frac{g}{6}(|c_4|^2 + |c_1|^2 + |c_2|^2)\Big)c_4 + \sqrt{3}\frac{g}{12}(c_4^* c_3)c_3 + \frac{g}{12}(c_1^* c_2)c_3$$
$$+ \frac{g}{12}(c_4^* c_2)c_2 + \frac{g}{12}(c_3^* c_1)c_2 + \frac{g}{12}(c_1^* c_3)c_2 + \frac{g}{12}(c_4^* c_2)c_1,$$

where the contributions from mixing terms have been symmetrized and evenly distributed across the equations for the four fields to ensure a balanced evolution of all components $\{c_\alpha\}$ during numerical calculations.

The system of Gross-Pitaevskii equations can be recasted in the form of a self-consistent eigenvalue problem

$$\mu c_\alpha = \sum_\beta H^{\mathrm{GP}}_{\alpha\beta}[\{c_\gamma\}]c_\beta, \quad (4.11)$$

where $H^{\mathrm{GP}}_{\alpha\beta}$ is the Gross-Pitaevskii Hamiltonian, constructed from the system of equations (4.10) and self-consistently depending on the fields $\{c_\alpha\}$. The explicit expression of $H^{\mathrm{GP}}_{\alpha\beta}$ is provided in Appendix C.1. The expression in (4.11) is a non-linear eigenvalue equation, in which we find c_α as the components of the fundamental eigenvector of the GP Hamiltonian and the chemical potential μ as fundamental eigenvalue. This is obtained within a self-consistent iterative algorithm: starting from an initial ansatz for the components $\{c^0_\alpha\}$, the Gross-Pitaevskii Hamiltonian $H^{\mathrm{GP}}[\{c^0_\alpha\}]$ is constructed and diagonalized. The resulting lowest energy eigenvector is then used to update the Hamiltonian, and the process is repeated until convergence to a stable ground-state solution is achieved. However, the Gross–Pitaevskii eigenvalue problem is highly non-linear and suffers from convergence issues when approached by direct diagonalization. Despite an extensive numerical search involving over $15{,}000$ randomized initial configurations, the eigenvalue method did not reach convergence in our system due to the large degeneracy of the classical ground-state manifold.

An alternative strategy which proves to be more efficient in our case is offered by dynamic evolution in imaginary time [61]. By moving from real to imaginary time through a Wick rotation $\tau = it$, Eq. (4.11) can be interpreted as a time-dependent Schrödinger equation for the wave-functions $\{c_\alpha\}$:

$$\partial_\tau \, c_\alpha = -\sum_\beta H^{\mathrm{GP}}_{\alpha\beta}[\{c_\gamma\}]c_\beta, \tag{4.12}$$

In this formulation, the ground state is reached as the steady state solution in the long-time limit:

$$\lim_{\tau\to\infty} c_\alpha(\tau) = c_\alpha^{\mathrm{gs}}. \tag{4.13}$$

This procedure does not require diagonalization, but only repeated applications of the Hamiltonian operator, and it is much more robust against functional energy fluctuations and degeneracy. Following the evolution of the wavefunction in imaginary time is in fact a way of implementing a minimization of the energy functional [61].

This minimization algorithm is numerically implemented by discretizing the time interval in infinitesimal steps $\delta\tau$, and updating the wavefunction at each time step via the first-order Euler scheme:

$$\mathbf{c}^{(n+1)} = \frac{(1-\delta\tau\, H^{\mathrm{GP}}[\{\mathbf{c}^{(n)}\}])\mathbf{c}^{(n)}}{\|(1-\delta\tau\, H^{\mathrm{GP}}[\{\mathbf{c}^{(n)}\}])\mathbf{c}^{(n)}\|}. \tag{4.14}$$

Here, $\mathbf{c}^{(n)}$ denotes the vector having components c_α at the time step $n\,\delta\tau$, with $\alpha = 1, 2, 3, 4$:

$$\mathbf{c} = \left[|c_1|\, e^{i\theta_{c_1}}, |c_2|\, e^{i\theta_{c_2}}, |c_3|\, e^{i\theta_{c_3}}, |c_4|\, e^{i\theta_{c_4}}\right], \tag{4.15}$$

and $H^{\mathrm{GP}}[\{\mathbf{c}^{(n)}\}]$ denotes the Gross–Pitaevskii Hamiltonian evaluated on the state at time step n. Since evolution in imaginary time is not unitary, the state is normalized at each step to avoid numerical divergences and preserve stability.

Starting from an initial ansatz $c_\alpha^{(0)}$, the Gross–Pitaevskii Hamiltonian is constructed and applied to evolve the system using Eq. (4.14). After each step, the classical energy functional Eq. (4.3) is evaluated. The procedure is iterated, updating H^{GP} at each step, until convergence is reached. Convergence is defined by monitoring the relative energy variation and stopping the evolution once it satisfies a chosen threshold, that we fixed to

$$\left|\frac{E_{n+1}-E_n}{E_n}\right| < 10^{-9}. \tag{4.16}$$

To identify the structure of the classical ground-state manifold, we run 3000 simulations with randomized initial conditions and fixed interaction strength $g = 10J$. Results of this numerical search lead to the identification of 12 competing minima in the four-mode condensate space. These minima are characterized

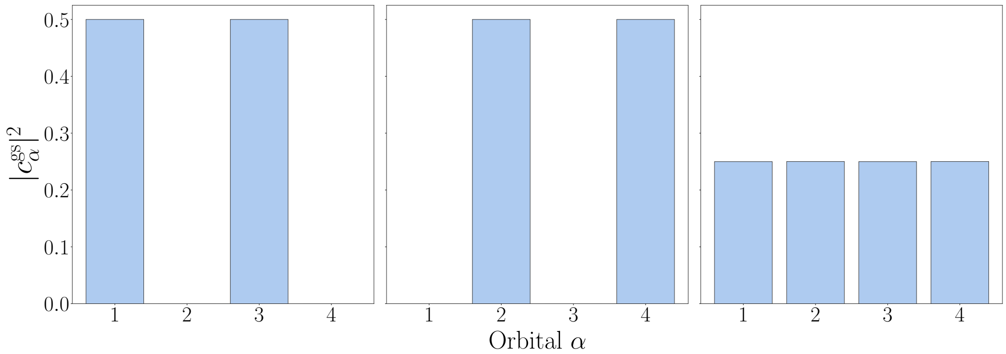

Figure 4.4: Density distinct configurations of the 12 classical ground states obtained from ITE. Each state is characterized either by uniform or localized orbital populations. All results correspond to $g = 10J$. The left and center panels show configurations with localized populations on orbitals $(1, 3)$ and $(2, 4)$, respectively. The right panel shows the ones with uniform orbital populations.

by different configurations of density distribution across the four orbitals, shown in Fig. 4.4, and of phase patterns:

- Four ground states are characterized by localized densities: two of them localized on orbitals $|c_1\rangle$ and $|c_3\rangle$, with relative phase difference $\theta_{c_1} - \theta_{c_3} = \pm\pi/2$,
$$\mathbf{c}_{1,2}^{\mathrm{gs}} = \left[\frac{1}{\sqrt{2}}, 0, \frac{1}{\sqrt{2}} e^{\pm i\frac{\pi}{2}}, 0\right], \tag{4.17}$$
and the other two with densities localized on orbitals $|c_2\rangle$ and $|c_4\rangle$ and phase difference $\theta_{c_2} - \theta_{c_4} = \pm\pi/2$,
$$\mathbf{c}_{3,4}^{\mathrm{gs}} = \left[0, \frac{1}{\sqrt{2}}, 0, \frac{1}{\sqrt{2}} e^{\pm i\frac{\pi}{2}}\right]. \tag{4.18}$$
Density configurations of these states are shown in the left and central panels of Fig. 4.4. Notice that in this case, upon fixing densities, the exact phase configurations $\Delta\theta = \pm\pi/2$ can be derived analytically by minimizing the energy functional in Eq. 4.3.
- Eight states characterized by uniform density distribution across the four orbitals,
$$\mathbf{c}_i^{\mathrm{gs}} = \left[\frac{1}{2}, \frac{1}{2} e^{i(\theta_2-\theta_1)}, \frac{1}{2} e^{i(\theta_3-\theta_1)}, \frac{1}{2} e^{i(\theta_4-\theta_1)}\right], \quad i = 5, \ldots, 12, \tag{4.19}$$
shown in the right panel of Fig. 4.4, and distinguished by complex phase patterns forming two sets of four chiral partners, visualized in Fig. 4.5.

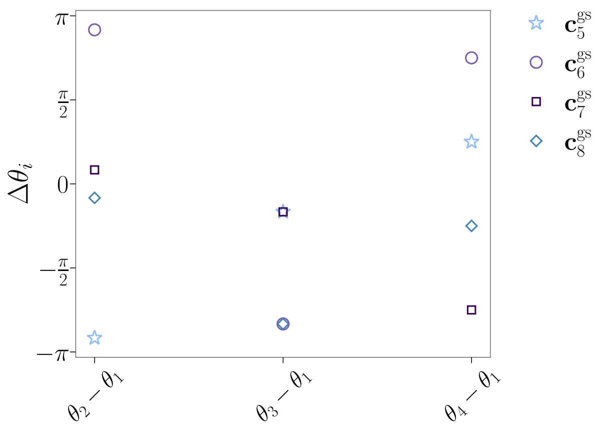

Figure 4.5: Phase patterns of one of the two sets of uniform-density ground states. The remaining four configurations are obtained by complex conjugation (chiral partners).

Analytical evaluation of the energy of the four density-localized configurations in Eqs. (4.17)–(4.18) via the energy functional in Eq. (4.3) yields

$$\frac{E_{\mathrm{MF}}[\{\mathbf{c}^{\mathrm{gs}}, \mathbf{c}^{\mathrm{gs}^*}\}] - E(N)}{N} = -\frac{g}{48}. \tag{4.20}$$

This agrees with the variational result E_{gs} of all the 12 numerical degenerate configurations

$$\frac{E_{\mathrm{gs}}}{J} \simeq -1.10705 \quad \text{for} \quad g = 10J. \tag{4.21}$$

It is worth noting that, in the four-mode effective theory, the coupling constant g appears as a global multiplicative prefactor in front of the interaction terms governing the dynamics, thus not entering in determining the ground state. As a consequence, the structure of the ground-state manifold for the projected theory is independent of g, and only the energy is rescaled. In the full eight-mode theory, instead, the parameter g competes with the finite gap $\propto J$ and this competition has a role in determining the ground state manifold. It is thus relevant to investigate the comparison between the classical ground states obtained from the projected and full Gross–Pitaevskii descriptions.

4.2.2 Gross-Pitaveskii description of the full theory

We now apply the formalism developed in the previous Section to study the classical ground states of the full eight-mode theory and compare them with those obtained from the projected model.

Starting from the full Hamiltonian in Eq. (3.1), with Bose–Hubbard interaction in normal-ordered form

$$\hat{H}_{\text{int}} = \frac{U}{2} \sum_{\alpha} \hat{b}^{\dagger}_{\alpha} \hat{b}^{\dagger}_{\alpha} \hat{b}_{\alpha} \hat{b}_{\alpha}, \tag{4.22}$$

we replace the bosonic operators with their classical coherent state expectation values,

$$\hat{b}_{\alpha} \to b_{\alpha} \equiv \langle \hat{b}_{\alpha} \rangle, \qquad \alpha = 1, \ldots, 8. \tag{4.23}$$

The resulting classical energy functional for the cubic cell reads

$$E_{\text{MF}}[\{b_{\alpha}, b^{*}_{\alpha}\}] = -\sum_{\langle \alpha\beta \rangle} J_{\alpha\beta}\, b^{*}_{\alpha} b_{\beta} + \frac{g}{2} \sum_{\alpha} |b_{\alpha}|^{4}, \tag{4.24}$$

where we have renormalized to the number of bosons $b_{\alpha} \to \sqrt{N}\, b_{\alpha}$, so that $\sum_{\alpha} |b_{\alpha}|^{2} = 1$, and $J_{\alpha\beta} = \pm J$ encodes the π-flux gauge structure (see Fig. 3.1). Assuming the standard *ansatz* for the classical fields

$$b_{\alpha} = |b_{\alpha}|\, e^{i\theta_{b_{\alpha}}}, \quad \alpha = 1, ..., 8, \tag{4.25}$$

the mean field energy per particle reads in terms of site densities and phase differences as:

$$\frac{E_{\text{MF}}[\{b_{\alpha}, b^{*}_{\alpha}\}]}{N} = -2J \sum_{\langle \alpha\beta \rangle} J_{\alpha\beta}\, |b_{\alpha}|\, |b_{\beta}| \cos\left(\theta_{b_{\alpha}} - \theta_{b_{\beta}}\right) + \frac{g}{2} \sum_{\alpha} |b_{\alpha}|^{4}. \tag{4.26}$$

The time-dependent Gross–Pitaevskii equation governing the classical dynamics

$$i\partial_t b_{\alpha} = \frac{\delta E_{\text{MF}}[b, b^{*}]}{\delta b^{*}_{\alpha}}, \tag{4.27}$$

admits the stationary solution

$$b_{\alpha}(t) = b^{(0)}_{\alpha} e^{-i\mu t}, \tag{4.28}$$

satisfying the stationary Gross–Pitaevskii equations

$$\mu b_{\alpha} = \frac{\delta E_{\text{MF}}[b, b^{*}]}{\delta b^{*}_{\alpha}}, \tag{4.29}$$

whose explicit form reads

$$\mu b_{\alpha} = -\sum_{i} J_{\alpha\beta}\, b_{\beta} + g\, |b_{\alpha}|^{2} b_{\alpha}. \tag{4.30}$$

This defines a system of eight coupled non-linear equations, which can be recast as a self-consistent eigenvalue problem:

$$i\partial_t \, b_\alpha = \mu \, b_\alpha = \sum_\beta H^{\mathrm{GP}}_{\alpha\beta}[\{b_\gamma\}]b_\beta, \tag{4.31}$$

where the Gross–Pitaevskii Hamiltonian $H^{\mathrm{GP}}_{\alpha\beta}$ depends self-consistently on the bosonic fields $\{b_\alpha\}$. The explicit structure of H^{GP} is derived from Eq. (4.30), and is reported in Appendix C.2.

To obtain the classical ground state manifold of the eight-mode model, we follow the same numerical strategy adopted for the projected theory: we solve the non-linear Gross–Pitaevskii eigenvalue problem by means of imaginary time evolution, interpreting the equations of motion as a time-dependent Schrödinger equation in imaginary time and evolving the state according to the iterative scheme introduced in Eq. (4.14).

The Gross–Pitaevskii Hamiltonian is updated at each step based on the current configuration of the classical fields, and convergence is reached up to the tolerance for the relative energy variation in Eq. (4.16).

We perform 3000 simulations with randomized initial conditions at fixed interaction strength $g = 10J$. All simulations converge to one of 12 distinct minima, characterized by uniform density distribution across the eight sites

$$\left|b^{\mathrm{gs}}_\alpha\right| \simeq \frac{1}{8}, \quad \alpha = 1, \ldots, 8, \tag{4.32}$$

within a numerical error of the order of 10^{-5}, and distinguished by 12 different complex phase configurations, pairly related by complex conjugation. For each of the above ground state configurations, we evaluate the particle current density along each bond connecting nearest-neighboring sites on the cubic unit cell, as defined by

$$j_{\alpha\beta} = i\left(J_{\alpha\beta}\, b^*_\alpha b_\beta - J^*_{\alpha\beta} b^*_\alpha b_\beta\right). \tag{4.33}$$

Here, the complex hopping $J_{\alpha\beta} = Je^{i\phi_{\alpha\beta}}$ encodes the π-flux structure through $\phi_{\alpha\beta} = 0, \pm\pi$ (see Fig. 3.1). Substituting the classical ansatz $b_\alpha = |b_\alpha|\, e^{i\theta_{b_\alpha}}$, the particle current density reads

$$j_{\alpha\beta} = 2J\,|b_\alpha|\,|b_\beta| \sin\left(\theta_{b_\alpha} - \theta_{b_\beta} + \phi_{\alpha\beta}\right). \tag{4.34}$$

Notably, each of the 12 ground states gives rise to a different closed pattern of density current, showing the emergence of chiral properties in the classical ground states. These current patterns form six distinct configurations, visualized in Fig. 4.6, the remaining six being their time-reversal partners. In particular,

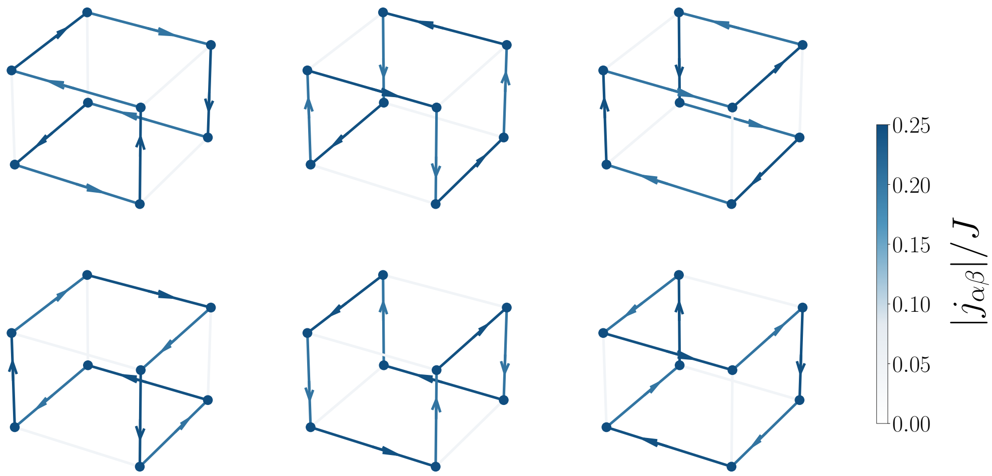

Figure 4.6: Loop-current patterns corresponding to six of the 12 classical ground states of the full eight-mode Gross–Pitaevskii theory. The remaining six are obtained by time reversal transformation. Each closed pattern corresponds to a minimum configuration with uniform density and non-zero particle current flowing on the edges of the π-flux cube.

we observe loop currents forming "chair"-like configurations on the faces of the cube. All 12 ground states are thus associated with non-zero loop currents, revealing the emergence of chiral order and spontaneous breaking of time-reversal symmetry in the classical limit. This is one of the main results of this Thesis and generalizes what observed in the two-dimensional case, where the interplay between frustration and interactions gives rise to local chiral currents and orbital order over the extended lattice.

A closer inspection of the 12 loop-current configurations reveals a structured organization under the crystalline symmetries of the cubic unit cell. In particular, each "chair"-current pattern can be mapped into one another by applying a gauge-dressed $\pi/2$-rotation [1] around the three principal axes, denoted in our notation as $\hat{C}_{4,\alpha}$ with $\alpha = x, y, z$, while none of them remains invariant under any of the $\hat{C}_{4,\alpha}$ operations. Each configuration, together with its time-reversal partner, is instead left invariant under a π-rotation $\hat{C}_{2,\alpha}$ around one of the three principal axes. Mirror operations $\hat{M}_\alpha$ act either as a reversal of all bond currents, mapping a pattern into its chiral partner, or as an effective $\hat{C}_{4,\alpha}$ operation that maps one configuration into another without reversing chirality.

This non-trivial behavior of loop current patterns under the action of crys-

[1] As discussed in Chapter 3, lattice transformations must be appropriately dressed by a gauge transformation to restore commutation with the single-particle Hamiltonian $\hat{H}_0$. Here the operator $\hat{C}_{4,\alpha}$ denotes the gauge-dressed $\pi/2$-rotation around the axis $\alpha = x, y, z$, acting on both the spatial and gauge structure of the hopping amplitudes, preserving the physical symmetry of the model.

talline transformations points out the role of crystalline symmetries in determining the algebraic structure underlying the ground state manifold, at least at a classical level. At a microscopic level, this observation points to a potential role of crystalline symmetries in the symmetry-protecting mechanisms responsible for the degeneracy structure in the many-body energy spectra discussed in the previous Section, suggesting further investigations on their role at finite fillings.

A next step in future studies is thus to understand how these classical states behave in the quantum regime: how quantum fluctuations lift the classical degeneracy, which subsets of states are selected, and how this selection depends on the particle filling.

Comparison with the projected theory

A last notable fact is that numerical results for the energy of the ground states coincide with the value obtained for the four-mode condensate in Eq. (4.21): all simulations of the full eight-mode model converge to the value $E_{\mathrm{gs}}/J \simeq -1.10705$ within the tolerance range defined in Eq. (4.16). This provides further validation of the effective theory in the range of interactions analyzed.

Moreover, we can compare the results of the full and projected theories by applying the unitary transformation defined in Eq. (3.21), which maps the low-energy modes of the eight-site model to the four effective orbitals, and vice versa. Each classical ground state $\mathbf{c}_{gs}$ obtained from the projected theory can thus be mapped into a configuration $\mathbf{b}$ in the full eight-dimensional space.

We find that each of all the classical ground states $\mathbf{c}_i^{\mathrm{gs}}$ of the four-orbital projected model maps onto a corresponding configuration $\mathbf{b}_{j(i)}^{\mathrm{gs}}$ obtained from the full eight-mode Gross–Pitaevskii variational analysis. A quantitative measure of this correspondence is given by the bounded Euclidean distance between the two eight-dimensional vectors

$$\| \widetilde{\mathcal{T}}\, \mathbf{c}_i^{\mathrm{gs}} - \mathbf{b}_{j(i)}^{\mathrm{gs}} \|^2 < 10^{-7} \quad \forall\, i = 1, \ldots, 12, \tag{4.35}$$

where $\widetilde{\mathcal{T}}$ is the 8×4 reduced matrix obtained from the unitary change–of–basis matrix $\mathcal{T}$ in Appendix B by selecting the columns corresponding to the lowest–energy subspace. This confirms that the two descriptions yield equivalent results, at least in the weakly interacting regime. The structure and degeneracy of the ground-state manifold are fully reproduced by the effective theory, demonstrating its validity in this regime.

We leave to future studies the investigation of how this agreement breaks down at stronger interaction strengths g, when the contribution of high-energy modes may no longer be negligible and the effective theory will fail in reproducing the correct low-energy physics.

5 Conclusions

The study presented in this Thesis aims to provide a theoretical investigation of a three-dimensional flux-frustrated Bose–Hubbard system, exploring the interacting bosonic BBH model on a single cubic plaquette pierced by a π-flux. By combining symmetry-based low-energy theory, exact diagonalization, and Gross–Pitaevskii analysis, this work shows how rich and non-trivial physics emerges in 3D flux-frustrated lattices by means of the interplay between geometric frustration, crystalline symmetries, and interactions in higher spatial dimensions. The highly regular structure of degeneracies and the strong filling dependence in the many-body energy spectrum are suggestive of hidden algebraic structures and are signal of a genuinely quantum phenomenon, revealing how the occupation number affects the structure of the interacting Hilbert space in the frustrated system, a feature that is surprisingly different from the 2D case. Based on the $SU(4)$ formulation provided in this work, a step forward in future investigations would be the full algebraic classification of the energy spectrum. Identifying the degeneracy-protecting symmetry and how it is modified by particle filling could open the way to understanding which type of orbital physics can emerge in the extended geometry and in the quantum limit.

As the main finding of this work, the highly degenerate classical ground-state manifold is characterized by the emergence of chiral order and spontaneous symmetry breaking in the weakly-interacting limit. Remarkably, each chiral ground state is associated with a closed loop-current pattern on the faces of the cube, with configurations related by time-reversal and crystalline symmetries. This result further generalizes what observed in the two-dimensional case: while closed loop-current states are typical and well-understood in 2D, the emergence of closed current patterns is more exotic in 3D systems, where the higher number of spatial degrees of freedom allows for the formation of non-trivial, more variegated patterns.

A first possible step in future studies is to go beyond the classical Gross–Pitaevskii description and determine how quantum fluctuations reshape the degenerate manifold, potentially lifting the classical degeneracy while stabilizing a selected subset of chiral ground states, alongside with the role of crystalline symmetries at finite filling in the quantum regime.

At the same time, an interesting perspective relies on the exploration of the extended lattice limit, scaling up the lattice by considering several π-flux cubes coupled by weak links, where the emergence of local chiral modes on the single cubic unit cell may lead to the emergence of macroscopic chiral currents over the extended lattice, signature of a topological non-trivial phase.

Connecting theory with ongoing experimental efforts, our model opens a novel direction for many-body physics in 3D flux-lattices and possibly introduces novel chiral states relevant for quantum simulation platforms.

A Derivation of Schwinger boson operators

In this appendix, we present the derivation of the $SU(2)$ Schwinger boson representation used in the effective theory developed in Chapter 2. This construction follows the Jordan–Schwinger map, which provides a direct correspondence between bosonic creation and annihilation operators and the generators of a finite-dimensional Lie algebra. Starting from the two-dimensional fundamental matrix representation of the Lie Algebra of $SU(2)$, the Jordan–Schwinger map allows to construct the corresponding Schwinger representation by associating each matrix generator to a bilinear operator in bosonic creation and annihilation operators. Specifically, for two bosonic mode operators $\hat{m}_1$ and $\hat{m}_2$, $SU(2)$ Schwinger operators are constructed as bilinear combinations of these bosonic operators:

$$\hat{J}_\mu = \frac{1}{2}\hat{m}_i^\dagger \left(\sigma^\mu\right)_{ij} \hat{m}_j \, , \tag{A.1}$$

where σ^μ are the Pauli matrices and the sum is over repeated indices. This yields Eq. (2.16) in the main text.

These bosonic operators satisfy the $SU(2)$ commutation relations by construction, being the Jordan-Schwinger map a homomorphism between representations, thus conserving the Lie bracket:

$$[\hat{J}^i, \hat{J}^j] = i\epsilon_{ijk}\hat{J}^k. \tag{A.2}$$

In this representation, the total particle number operator

$$\hat{n} = \hat{m}_1^\dagger \hat{m}_1 + \hat{m}_2^\dagger \hat{m}_2 \, , \tag{A.3}$$

acts as the Casimir operator of the algebra, commuting with all $\hat{J}^i$:

$$[\hat{n}, \hat{J}^i] = 0\,, \tag{A.4}$$

and sets the total angular momentum value for a given irreducible representation. Specifically, the Casimir operator is given by:

$$\hat{C} = \hat{J}^2 = \hat{J}_x^2 + \hat{J}_y^2 + \hat{J}_z^2\,, \tag{A.5}$$

and its eigenvalue is related to the total particle number by:

$$\hat{C} = \frac{\hat{n}}{2}\left(\frac{\hat{n}}{2} + 1\right). \tag{A.6}$$

The eigenstates of the system are thus labeled by the total number of bosons $\hat{n}$ and the angular momentum projections associated with the $SU(2)$ operators.

By applying the Jordan–Schwinger map to the two-mode bosonic system, we obtain an effective angular momentum description that connects the low-energy modes $\hat{m}_1$ and $\hat{m}_2$ to an emergent $SU(2)$ algebra. This derivation provides the effective Hamiltonian used in Chapter 2, where the emergent p-orbital degrees of freedom and their interactions can be recast as angular momentum interactions within the Schwinger boson formalism.

For a detailed derivation and generalization to multi-mode systems, we refer to the formalism presented in Ref. [51].

B Simultaneous diagonalization and projection onto the low-energy sector

In this appendix, we present the diagonalization of the single-particle Hamiltonian $\hat{H}_0$ together with a maximal commuting subset of dressed crystalline symmetries, and describe how the effective low-energy theory is obtained via projection onto the degenerate ground-state manifold.

Among the crystalline symmetries of the cubic lattice, we consider the set of dressed symmetry operators $\hat{M}_z, \hat{C}_{2,z}$, which satisfy the mutual commutation relations:

$$[\hat{H}_0, \hat{M}_z] = [\hat{H}_0, \hat{C}_{2,z}] = [\hat{M}_z, \hat{C}_{2,z}] = 0. \tag{B.1}$$

The single-particle Hamiltonian $\hat{H}_0$ on the eight-site cubic unit cell is represented in the $\{|b_j\rangle\}$ single-particle basis by an 8×8 Hermitian matrix, whose entries encode the hopping amplitudes between the sites of the cubic unit cell:

$$\hat{H}_0 = \begin{pmatrix} 0 & 1 & -1 & 0 & -1 & 0 & 0 & 0 \\ 1 & 0 & 0 & -1 & 0 & -1 & 0 & 0 \\ -1 & 0 & 0 & -1 & 0 & 0 & 1 & 0 \\ 0 & -1 & -1 & 0 & 0 & 0 & 0 & -1 \\ -1 & 0 & 0 & 0 & 0 & -1 & -1 & 0 \\ 0 & -1 & 0 & 0 & -1 & 0 & 0 & 1 \\ 0 & 0 & 1 & 0 & -1 & 0 & 0 & -1 \\ 0 & 0 & 0 & -1 & 0 & 1 & -1 & 0 \end{pmatrix}. \tag{B.2}$$

Symmetry operators $\hat{M}_z$ and $\hat{C}_{2,z}$ are represented in matrix form in the same basis as

$$
\hat{M}_z = \begin{pmatrix}
0 & 1 & 0 & 0 & 0 & 0 & 0 & 0 \\
1 & 0 & 0 & 0 & 0 & 0 & 0 & 0 \\
0 & 0 & 0 & 1 & 0 & 0 & 0 & 0 \\
0 & 0 & 1 & 0 & 0 & 0 & 0 & 0 \\
0 & 0 & 0 & 0 & 0 & 1 & 0 & 0 \\
0 & 0 & 0 & 0 & 1 & 0 & 0 & 0 \\
0 & 0 & 0 & 0 & 0 & 0 & 0 & -1 \\
0 & 0 & 0 & 0 & 0 & 0 & -1 & 0
\end{pmatrix}, \tag{B.3}
$$

$$
\hat{C}_{2,z} = \begin{pmatrix}
0 & 0 & 0 & 0 & 0 & 0 & 1 & 0 \\
0 & 0 & 0 & 0 & 0 & 0 & 0 & -1 \\
0 & 0 & 0 & 0 & 1 & 0 & 0 & 0 \\
0 & 0 & 0 & 0 & 0 & 1 & 0 & 0 \\
0 & 0 & -1 & 0 & 0 & 0 & 0 & 0 \\
0 & 0 & 0 & -1 & 0 & 0 & 0 & 0 \\
-1 & 0 & 0 & 0 & 0 & 0 & 0 & 0 \\
0 & 1 & 0 & 0 & 0 & 0 & 0 & 0
\end{pmatrix}. \tag{B.4}
$$

The simultaneous diagonalization of the three operators is realized via the unitary matrix $\mathcal{T}$

$$
\mathcal{T} = \frac{1}{A} \begin{pmatrix}
-z & -z^* & zB & z^*B & z^*B & zB & -z^* & -z \\
z & z^* & zB & z^*B & -z^*B & -zB & -z^* & -z \\
-B & -B & 1 & 1 & -1 & -1 & B & B \\
B & B & 1 & 1 & 1 & 1 & B & B \\
-iB & iB & i & -i & i & -i & -iB & iB \\
iB & -iB & i & -i & -i & i & -iB & iB \\
z^* & z & -z^*B & -zB & -zB & -z^*B & z & z^* \\
z^* & z & z^*B & zB & -zB & -z^*B & -z & -z^*
\end{pmatrix}, \tag{B.5}
$$

where

$$
\begin{aligned}
z &= e^{i\frac{\pi}{4}}, \\
A &= 2\sqrt{3-\sqrt{3}}, \\
B &= \frac{\sqrt{3}-1}{\sqrt{2}},
\end{aligned} \tag{B.6}
$$

such that

$$\hat{H}_0^{\text{diag}} = \mathcal{T}^{-1}\hat{H}_0\mathcal{T} = \begin{pmatrix} -\sqrt{3} & 0 & 0 & 0 & 0 & 0 & 0 & 0 \\ 0 & -\sqrt{3} & 0 & 0 & 0 & 0 & 0 & 0 \\ 0 & 0 & -\sqrt{3} & 0 & 0 & 0 & 0 & 0 \\ 0 & 0 & 0 & -\sqrt{3} & 0 & 0 & 0 & 0 \\ 0 & 0 & 0 & 0 & \sqrt{3} & 0 & 0 & 0 \\ 0 & 0 & 0 & 0 & 0 & \sqrt{3} & 0 & 0 \\ 0 & 0 & 0 & 0 & 0 & 0 & \sqrt{3} & 0 \\ 0 & 0 & 0 & 0 & 0 & 0 & 0 & \sqrt{3} \end{pmatrix}, \tag{B.7}$$

$$\hat{M}_z^{\text{diag}} = \mathcal{T}^{-1}\hat{M}_z\mathcal{T} = \begin{pmatrix} -1 & 0 & 0 & 0 & 0 & 0 & 0 & 0 \\ 0 & -1 & 0 & 0 & 0 & 0 & 0 & 0 \\ 0 & 0 & 1 & 0 & 0 & 0 & 0 & 0 \\ 0 & 0 & 0 & 1 & 0 & 0 & 0 & 0 \\ 0 & 0 & 0 & 0 & -1 & 0 & 0 & 0 \\ 0 & 0 & 0 & 0 & 0 & -1 & 0 & 0 \\ 0 & 0 & 0 & 0 & 0 & 0 & 1 & 0 \\ 0 & 0 & 0 & 0 & 0 & 0 & 0 & 1 \end{pmatrix}, \tag{B.8}$$

$$\hat{C}_{2,z}^{\text{diag}} = \mathcal{T}^{-1}C_{2,z}\mathcal{T} = \begin{pmatrix} i & 0 & 0 & 0 & 0 & 0 & 0 & 0 \\ 0 & -i & 0 & 0 & 0 & 0 & 0 & 0 \\ 0 & 0 & i & 0 & 0 & 0 & 0 & 0 \\ 0 & 0 & 0 & -i & 0 & 0 & 0 & 0 \\ 0 & 0 & 0 & 0 & -i & 0 & 0 & 0 \\ 0 & 0 & 0 & 0 & 0 & i & 0 & 0 \\ 0 & 0 & 0 & 0 & 0 & 0 & -i & 0 \\ 0 & 0 & 0 & 0 & 0 & 0 & 0 & i \end{pmatrix}. \tag{B.9}$$

The columns of $\mathcal{T}$ define the new basis of symmetry-adapted single-particle eigenstates $|c_i\rangle$:

$$|c_i\rangle = \sum_j \mathcal{T}_{ij}^{-1} |b_j\rangle \,. \tag{B.10}$$

From the diagonal form of $\hat{H}_0$, the degenerate ground-state manifold is spanned by the eigenmodes $\{|c_1\rangle, |c_2\rangle, |c_3\rangle, |c_4\rangle\}$ with energy $-\sqrt{3}J$. The projection onto the low-energy subspace is performed by restricting to this four-dimensional sector: by decomposing bosonic operators in the original basis via the unitary transformation $\hat{b}_i = \sum_j \mathcal{T}_{ij}\hat{c}_j$, and by dropping the contribution from the higher energy modes $\{\hat{c}_5, \hat{c}_6, \hat{c}_7, \hat{c}_8\}$.

The Hubbard interaction

$$\hat{H}_{\text{int}} = \frac{U}{2}\sum_i \hat{b}_i^\dagger \hat{b}_i^\dagger \hat{b}_i \hat{b}_i, \tag{B.11}$$

becomes

$$\begin{aligned}
\hat{H}_{\text{int}}^{\text{eff}} \equiv \hat{\mathcal{P}}\hat{H}_{\text{int}}\hat{\mathcal{P}} =& \frac{U}{12}(\hat{c}_1^\dagger\hat{c}_1^\dagger\hat{c}_1\hat{c}_1 + \hat{c}_2^\dagger\hat{c}_2^\dagger\hat{c}_2\hat{c}_2 + \hat{c}_3^\dagger\hat{c}_3^\dagger\hat{c}_3\hat{c}_3 + \hat{c}_4^\dagger\hat{c}_4^\dagger\hat{c}_4\hat{c}_4) \\
&+ \frac{U}{3}(\hat{c}_1^\dagger\hat{c}_2^\dagger\hat{c}_1\hat{c}_2 + \hat{c}_3^\dagger\hat{c}_4^\dagger\hat{c}_3\hat{c}_4) \\
&+ \frac{U}{6}(\hat{c}_1^\dagger\hat{c}_3^\dagger\hat{c}_1\hat{c}_3 + \hat{c}_2^\dagger\hat{c}_3^\dagger\hat{c}_2\hat{c}_3 + \hat{c}_1^\dagger\hat{c}_4^\dagger\hat{c}_1\hat{c}_4 + \hat{c}_2^\dagger\hat{c}_4^\dagger\hat{c}_2\hat{c}_4) \\
&-\sqrt{3}\frac{U}{24}(\hat{c}_1^\dagger\hat{c}_1^\dagger\hat{c}_2\hat{c}_2 + \hat{c}_2^\dagger\hat{c}_2^\dagger\hat{c}_1\hat{c}_1) + \sqrt{3}\frac{U}{24}(\hat{c}_3^\dagger\hat{c}_3^\dagger\hat{c}_4\hat{c}_4 + \hat{c}_4^\dagger\hat{c}_4^\dagger\hat{c}_3\hat{c}_3) \\
&+ \frac{U}{24}(\hat{c}_1^\dagger\hat{c}_1^\dagger\hat{c}_3\hat{c}_3 + \hat{c}_3^\dagger\hat{c}_3^\dagger\hat{c}_1\hat{c}_1 + \hat{c}_2^\dagger\hat{c}_2^\dagger\hat{c}_4\hat{c}_4 + \hat{c}_4^\dagger\hat{c}_4^\dagger\hat{c}_2\hat{c}_2) \\
&+ \frac{U}{6}(\hat{c}_1^\dagger\hat{c}_2^\dagger\hat{c}_3\hat{c}_4 + \hat{c}_3^\dagger\hat{c}_4^\dagger\hat{c}_1\hat{c}_2 + \hat{c}_1^\dagger\hat{c}_4^\dagger\hat{c}_3\hat{c}_2 + \hat{c}_3^\dagger\hat{c}_2^\dagger\hat{c}_1\hat{c}_4).
\end{aligned} \tag{B.12}$$

Defining $\hat{n}_i = \hat{c}_i^\dagger\hat{c}_i$ as the occupation of orbital i, and using bosonic commutation relations $[\hat{c}_i, \hat{c}_j^\dagger] = \delta_{ij}$, the interaction Hamiltonian in Eq. (B.12) leads to the expression in Eq. (3.26) in the main text.

C Details of the Gross-Pitaevskii simulations

This Appendix provides additional technical details and explicit expressions used in the Gross–Pitaevskii (GP) analysis discussed in Chapter 4. In both the four-mode effective theory and the full eight-mode model, the classical ground states are obtained by solving the stationary Gross–Pitaevskii equations via imaginary time evolution. We report here the full expressions of the GP Hamiltonians governing the evolutions, which are constructed from the stationary equations and define the update rules used in the numerical procedure, and present the resulting density distributions of the converged states over 3000 independent simulations at fixed interaction strength $g = 10J$, providing a measure of the convergence of the method.

C.1 Four-mode theory

The GP equations for the four-mode effective theory, derived from the energy functional (4.3), are reported explicitly in Eq. (4.10) of the main text. These define a set of coupled non-linear equations for the classical fields $\{c_\alpha\}$, from which we construct the effective GP Hamiltonian $H^{\mathrm{GP}}_{\mathrm{eff}}$ appearing in the eigenvalue problem in Eq. (4.11):

$$H^{\mathrm{GP}}_{\mathrm{eff}} = (H^{\mathrm{GP}}_{\alpha\beta})^{4}_{\alpha,\beta=1}, \tag{C.1}$$

whose independent matrix elements read:

$$\begin{aligned}
H^{\mathrm{GP}}_{11} &= -\sqrt{3}J + \frac{g}{3}|c_2|^2 + \frac{g}{6}(|c_1|^2 + |c_3|^2 + |c_4|^2), \\
H^{\mathrm{GP}}_{12} &= -\sqrt{3}\frac{g}{12}c_1^* c_2 + \frac{g}{12}c_4^* c_3, \\
H^{\mathrm{GP}}_{13} &= \frac{g}{12}(c_1^* c_3 + c_4^* c_2 + c_2^* c_4),
\end{aligned}$$

$$
\begin{aligned}
H_{14}^{\mathrm{GP}} &= \frac{g}{12} c_2^* c_3, \\
H_{22}^{\mathrm{GP}} &= -\sqrt{3} J + \frac{g}{3} |c_1|^2 + \frac{g}{6} \left(|c_2|^2 + |c_3|^2 + |c_4|^2 \right), \\
H_{23}^{\mathrm{GP}} &= \frac{g}{12}\, c_1^* c_4, \\
H_{24}^{\mathrm{GP}} &= \frac{g}{12} \left(c_2^* c_4 + c_1^* c_3 + c_3^* c_1 \right), \\
H_{33}^{\mathrm{GP}} &= -\sqrt{3} J + \frac{g}{3} |c_4|^2 + \frac{g}{6} \left(|c_1|^2 + |c_2|^2 + |c_3|^2 \right), \\
H_{34}^{\mathrm{GP}} &= \sqrt{3}\, \frac{g}{12}\, c_3^* c_4 + \frac{g}{12}\, c_2^* c_1, \\
H_{44}^{\mathrm{GP}} &= -\sqrt{3} J + \frac{g}{3} |c_3|^2 + \frac{g}{6} \left(|c_1|^2 + |c_2|^2 + |c_4|^2 \right),
\end{aligned} \tag{C.2}
$$

the remaining elements following from Hermiticity as $H_{ji}^{\mathrm{GP}} = (H_{ij}^{\mathrm{GP}})^*$. This is the Hamiltonian numerically implemented in the first-order evolution scheme defined in Eq. (4.14) used to approach the ground state.

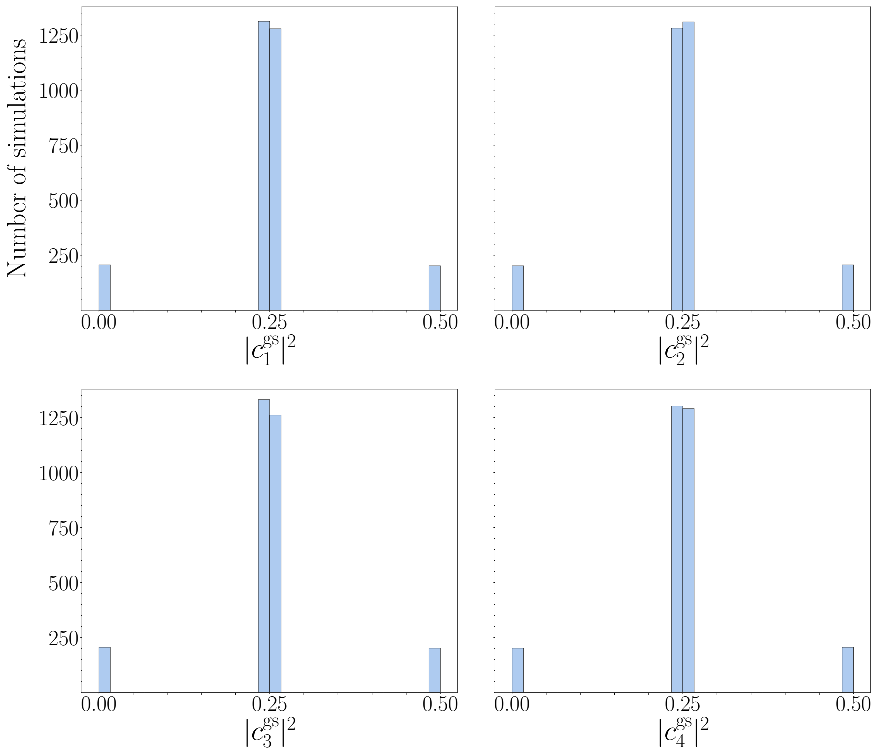

Figure C.1: Orbital density distribution $|c_\alpha^{\mathrm{gs}}|^2$ resulting from 3000 simulations of the GP dynamics in the effective four-mode theory at $g = 10J$. Each panel corresponds to one of the four orbitals.

Fig. C.1 shows the resulting density distributions $|c_\alpha^{\mathrm{gs}}|^2$ of the 3000 converged states for each orbital component. The sharp peaks and narrow distributions centered at values $|c_\alpha^{\mathrm{gs}}|^2 = 0, \frac{1}{4}, \frac{1}{2}$ confirm the convergence and stability of the method.

C.2 Eight-mode theory

We follow the same procedure to determine the classical ground state manifold arising from the Gross-Pitaevskii description of the eight-mode condensate. The system of stationary GP equations for the classical fields $\{b_\alpha\}$,

$$
\begin{aligned}
\mu\, b_1 &= \frac{\delta E_{\mathrm{MF}}}{\delta b_1^*} = -J\big(e^{i\pi} b_2 + b_3 + b_5\big) + g\,|b_0|^2 b_0, \\
\mu\, b_2 &= \frac{\delta E_{\mathrm{MF}}}{\delta b_2^*} = -J\big(b_4 + b_6 + e^{-i\pi} b_1\big) + g\,|b_2|^2 b_2, \\
\mu\, b_3 &= \frac{\delta E_{\mathrm{MF}}}{\delta b_3^*} = -J\big(b_1 + b_4 + e^{-i\pi} b_7\big) + g\,|b_3|^2 b_3, \\
\mu\, b_4 &= \frac{\delta E_{\mathrm{MF}}}{\delta b_4^*} = -J\big(b_3 + b_8 + b_2\big) + g\,|b_4|^2 b_4, \\
\mu\, b_5 &= \frac{\delta E_{\mathrm{MF}}}{\delta b_5^*} = -J\big(b_1 + b_6 + b_7\big) + g\,|b_5|^2 b_5, \\
\mu\, b_6 &= \frac{\delta E_{\mathrm{MF}}}{\delta b_6^*} = -J\big(b_5 + e^{-i\pi} b_8 + b_2\big) + g\,|b_6|^2 b_6, \\
\mu\, b_7 &= \frac{\delta E_{\mathrm{MF}}}{\delta b_7^*} = -J\big(b_8 + e^{i\pi} b_3 + b_5\big) + g\,|b_7|^2 b_7, \\
\mu\, b_8 &= \frac{\delta E_{\mathrm{MF}}}{\delta b_8^*} = -J\big(e^{i\pi} b_6 + b_7 + b_4\big) + g\,|b_8|^2 b_8,
\end{aligned}
\tag{C.3}
$$

defines the eight-dimensional GP Hamiltonian

$$
H^{\mathrm{GP}} = \begin{pmatrix}
g|b_1|^2 & J & -J & 0 & -J & 0 & 0 & 0 \\
J & g|b_2|^2 & 0 & -J & 0 & -J & 0 & 0 \\
-J & 0 & g|b_3|^2 & -J & 0 & 0 & J & 0 \\
0 & -J & -J & g|b_4|^2 & 0 & 0 & 0 & -J \\
-J & 0 & 0 & 0 & g|b_5|^2 & -J & -J & 0 \\
0 & -J & 0 & 0 & -J & g|b_6|^2 & 0 & J \\
0 & 0 & J & 0 & -J & 0 & g|b_7|^2 & -J \\
0 & 0 & 0 & -J & 0 & J & -J & g|b_8|^2
\end{pmatrix}, \tag{C.4}
$$

whose imaginary-time dynamics, implemented through the evolution scheme in Section 4.2.2, leads to the identification of a twelvefold degenerate manifold of minima, characterized by uniform density distribution across the eight sites of the cubic unit cell. The density distributions from 3000 simulations at $g = 10J$ are displayed in Fig. C.2. Each site shows a sharp peak centered at $|b_\alpha^{\mathrm{gs}}|^2 = \frac{1}{8}$, again confirming convergence and accuracy of the ITE algorithm.

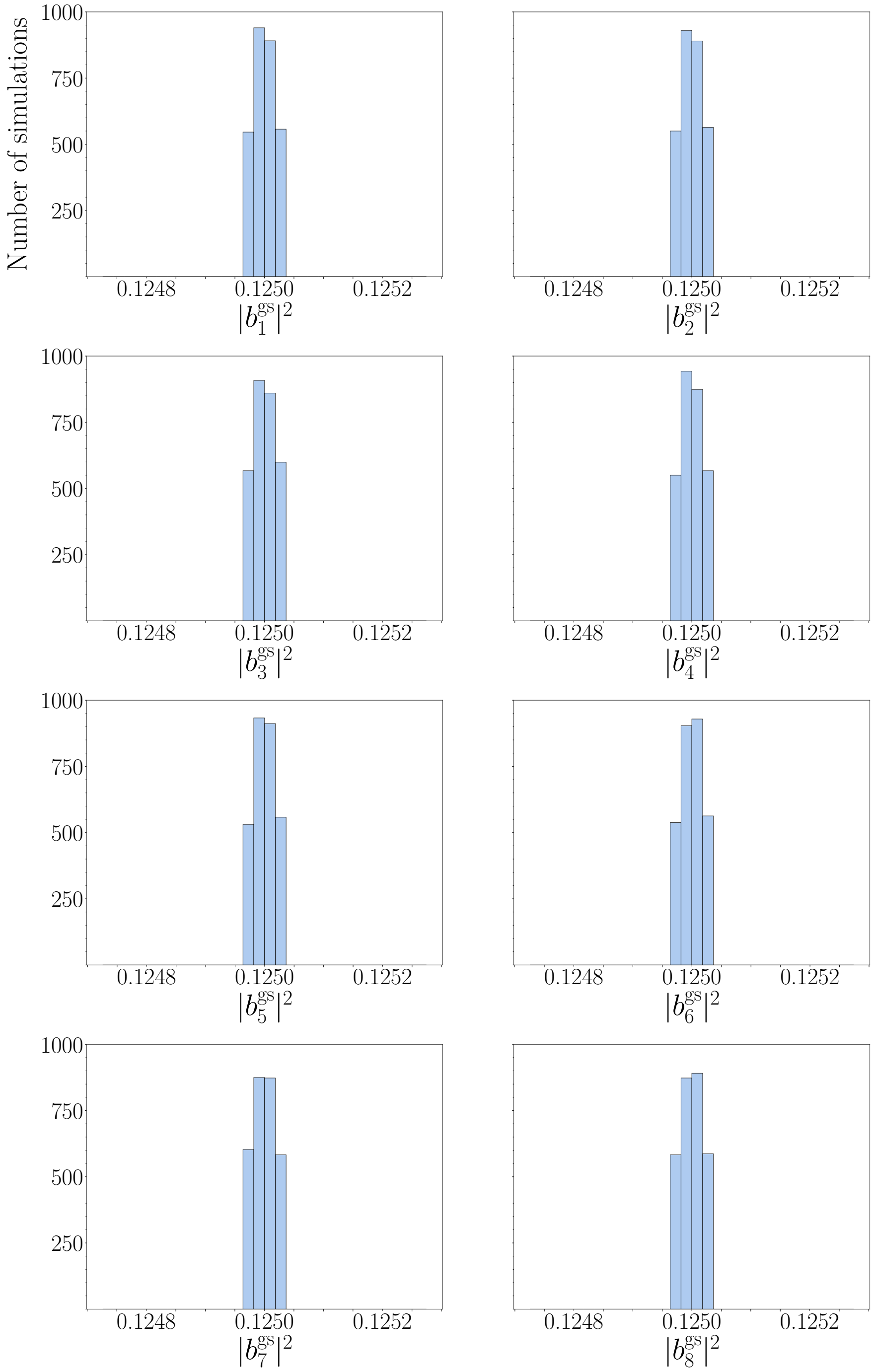

Figure C.2: Density distributions $|b_\alpha^{\mathrm{gs}}|^2$ for each of the eight sites, resulting from 3000 simulations of the full Gross–Pitaevskii dynamics at $g = 10J$. Each site converges to uniform average density, with minimal fluctuations.

Bibliography

[1] X. G. Wen, *Quantum Field Theory of Many-Body Systems: From the Origin of Sound to an Origin of Light and Electrons* (Oxford University Press, 2007).

[2] R. E. Prange and S. M. Girvin, *The Quantum Hall Effect*, 2nd ed., Graduate Texts in Contemporary Physics (Springer, 1990).

[3] K. v. Klitzing, G. Dorda, and M. Pepper, "New method for high-accuracy determination of the fine-structure constant based on quantized Hall resistance", Phys. Rev. Lett. **45**, 494–497 (1980).

[4] D. C. Tsui, H. L. Stormer, and A. C. Gossard, "Two-dimensional magnetotransport in the extreme quantum limit", Phys. Rev. Lett. **48**, 1559–1562 (1982).

[5] R. B. Laughlin, "Anomalous Quantum Hall Effect: An Incompressible Quantum Fluid with Fractionally Charged Excitations", Phys. Rev. Lett. **50**, 1395–1398 (1983).

[6] X. G. Wen and Q. Niu, "Ground-state degeneracy of the fractional quantum Hall states in the presence of a random potential and on high-genus Riemann surfaces", Phys. Rev. B **41**, 9377–9396 (1990).

[7] D. J. Thouless, M. Kohmoto, M. P. Nightingale, and M. den Nijs, "Quantized Hall conductance in a two-dimensional periodic potential", Phys. Rev. Lett. **49**, 405–408 (1982).

[8] R. P. Feynman, "Simulating physics with computers", Int. J. Theor. Phys. **21**, 467–488 (1982).

[9] I. Bloch, J. Dalibard, and W. Zwerger, "Many-body physics with ultracold gases", Rev. Mod. Phys. **80**, 885–964 (2008).

[10] I. Bloch, J. Dalibard, and S. Nascimbène, "Quantum simulations with ultracold quantum gases", Nat. Phys. **8**, 267–276 (2012).

[11] M. Lewenstein, A. Sanpera, V. Ahufinger, B. Damski, A. Sen(De), and U. Sen, "Ultracold atomic gases in optical lattices: mimicking condensed matter physics and beyond", Adv. Phys. **56**, 243–379 (2007).

[12] D. Jaksch, C. Bruder, J. I. Cirac, C. W. Gardiner, and P. Zoller, "Cold bosonic atoms in optical lattices", Phys. Rev. Lett. **81**, 3108–3111 (1998).

[13] D. Jaksch and P. Zoller, "The cold atom Hubbard toolbox", Ann. Phys. **315**, 52–79 (2005).

[14] M. Greiner and S. Fölling, "Optical lattices", Nature **453**, 736–738 (2008).

[15] C. Gross and I. Bloch, "Quantum simulations with ultracold atoms in optical lattices", Science **357**, 995–1001 (2017).

[16] M. P. A. Fisher, P. B. Weichman, G. Grinstein, and D. S. Fisher, "Boson localization and the superfluid-insulator transition", Phys. Rev. B **40**, 546–570 (1989).

[17] M. Greiner, O. Mandel, T. Esslinger, T. W. Hänsch, and I. Bloch, "Quantum phase transition from a superfluid to a Mott insulator in a gas of ultracold atoms", Nature **415**, 39–44 (2002).

[18] J. Dalibard, F. Gerbier, G. Juzeliūnas, and P. Öhberg, "Colloquium: Artificial gauge potentials for neutral atoms", Rev. Mod. Phys. **83**, 1523–1543 (2011).

[19] N. Goldman, G. Juzeliūnas, P. Öhberg, and I. B. Spielman, "Light-induced gauge fields for ultracold atoms", Rep. Prog. Phys. **77**, 126401 (2014).

[20] M. Aidelsburger, S. Nascimbène, and N. Goldman, "Artificial gauge fields in materials and engineered systems", C. R. Phys. **19**, 394–432 (2018).

[21] N. Goldman, J. C. Budich, and P. Zoller, "Topological quantum matter with ultracold gases in optical lattices", Nat. Phys. **12**, 639–645 (2016).

[22] N. R. Cooper, J. Dalibard, and I. B. Spielman, "Topological bands for ultracold atoms", Rev. Mod. Phys. **91**, 015005 (2019).

[23] D. R. Hofstadter, "Energy levels and wave functions of Bloch electrons in rational and irrational magnetic fields", Phys. Rev. B **14**, 2239–2249 (1976).

[24] M. Aidelsburger, M. Atala, M. Lohse, J. T. Barreiro, B. Paredes, and I. Bloch, "Realization of the Hofstadter Hamiltonian with Ultracold Atoms in Optical Lattices", Phys. Rev. Lett. **111**, 185301 (2013).

[25] A. S. Sørensen, E. Demler, and M. D. Lukin, "Fractional quantum hall states of atoms in optical lattices", Phys. Rev. Lett. **94**, 086803 (2005).

[26] M. Hafezi, A. S. Sørensen, E. Demler, and M. D. Lukin, “Fractional quantum Hall effect in optical lattices”, Phys. Rev. A **76**, 023613 (2007).

[27] G. Möller and N. R. Cooper, “Composite fermion theory for bosonic quantum hall states on lattices”, Phys. Rev. Lett. **103**, 105303 (2009).

[28] J. Léonard, S. Kim, J. Kwan, P. Segura, F. Grusdt, C. Repellin, N. Goldman, and M. Greiner, “Realization of a fractional quantum Hall state with ultracold atoms”, Nature **619**, 495–499 (2023).

[29] F. D. M. Haldane, “Model for a Quantum Hall Effect without Landau Levels: Condensed-Matter Realization of the "Parity Anomaly"”, Phys. Rev. Lett. **61**, 2015–2018 (1988).

[30] G. Jotzu, M. Messer, R. Desbuquois, M. Lebrat, T. Uehlinger, D. Greif, and T. Esslinger, “Experimental realization of the topological Haldane model with ultracold fermions”, Nature **515**, 237–240 (2014).

[31] N. Regnault and B. A. Bernevig, “Fractional Chern insulator”, Phys. Rev. X **1**, 021014 (2011).

[32] T. Neupert, L. Santos, C. Chamon, and C. Mudry, “Fractional Quantum Hall States at Zero Magnetic Field”, Phys. Rev. Lett. **106**, 236804 (2011).

[33] G. Möller and N. R. Cooper, “Correlated phases of bosons in the flat lowest band of the Dice lattice”, Phys. Rev. Lett. **108**, 045306 (2012).

[34] G. Wirth, M. Ölschläger, and A. Hemmerich, “Evidence for orbital superfluidity in the P-band of a bipartite optical square lattice”, Nat. Phys. **7**, 147–153 (2011).

[35] M. Di Liberto and N. Goldman, “Chiral orbital order of interacting bosons without higher bands”, Phys. Rev. Research **5**, 023064 (2023).

[36] X. Li and W. V. Liu, “Physics of higher orbital bands in optical lattices: a review”, Rep. Prog. Phys. **79**, 116401 (2016).

[37] Z. Cai, Y. Wang, and C. Wu, “Frustrated Bose-Einstein condensates with noncollinear orbital ordering”, Phys. Rev. B **86**, 060517 (2012).

[38] W. V. Liu and C. Wu, “Atomic matter of nonzero-momentum Bose-Einstein condensation and orbital current order”, Phys. Rev. A **74**, 013607 (2006).

[39] A. Isacsson and S. M. Girvin, “Multiflavor bosonic Hubbard models in the first excited Bloch band of an optical lattice”, Phys. Rev. A **72**, 053604 (2005).

[40] W. A. Benalcazar, B. A. Bernevig, and T. L. Hughes, “Quantized electric multipole insulators”, Science **357**, 61–66 (2017).

[41] F. Schindler, A. M. Cook, M. G. Vergniory, Z. Wang, S. S. P. Parkin, B. A. Bernevig, and T. Neupert, “Higher-order topological insulators”, Sci. Adv. **4**, eaat0346 (2018).

[42] A. Impertro, S. Huh, S. Karch, J. F. Wienand, I. Bloch, and M. Aidelsburger, “Strongly interacting Meissner phases in large bosonic flux ladders”, Nat. Phys. **21**, 895–901 (2025).

[43] W. A. Benalcazar, B. A. Bernevig, and T. L. Hughes, “Electric multipole moments, topological multipole moment pumping, and chiral hinge states in crystalline insulators”, Phys. Rev. B **96**, 245115 (2017).

[44] W. P. Su, J. R. Schrieffer, and A. J. Heeger, “Solitons in polyacetylene”, Phys. Rev. Lett. **42**, 1698–1701 (1979).

[45] J. K. Asbóth, L. Oroszlány, and A. Pályi, *A Short Course on Topological Insulators*, Vol. 919 (Springer, 2016).

[46] M. Ölschläger, T. Kock, G. Wirth, A. Ewerbeck, C. Morais Smith, and A. Hemmerich, “Interaction-induced chiral $p_x \pm ip_y$ superfluid order of bosons in an optical lattice”, New J. Phys. **15**, 083041 (2013).

[47] T. Kock, C. Hippler, A. Ewerbeck, and A. Hemmerich, “Orbital optical lattices with bosons”, J. Phys. B: At. Mol. Opt. Phys. **49**, 042001 (2016).

[48] X. Li, E. Zhao, and W. V. Liu, “Topological states in a ladder-like optical lattice containing ultracold atoms in higher orbital bands”, Nat. Commun. **4**, 1523 (2013).

[49] A. Klein and E. R. Marshalek, “Boson realizations of Lie algebras with applications to nuclear physics”, Rev. Mod. Phys. **63**, 375–558 (1991).

[50] J. Schwinger, *On Angular Momentum*, NYO-3071 (U.S. Atomic Energy Commission, 1952).

[51] B. Dubus, T. Haas, and N. J. Cerf, “From bosons and fermions to spins: a multi-mode extension of the Jordan–Schwinger map”, arXiv preprint arXiv:2411.04918, 2024.

[52] A. Leviatan, “Partial dynamical symmetries”, Prog. Part. Nucl. Phys. **66**, 93–143 (2011).

[53] F. Iachello, *Lie Algebras and Applications*, Vol. 708 (Springer, 2006).

[54] W. Greiner, *Relativistic Quantum Mechanics: Wave Equations*, 3rd ed. (Springer, 2000).

[55] S. Weinberg, *The Quantum Theory of Fields*, Vol. 2 (Cambridge University Press, 1995).

[56] W. Pfeifer, *The Lie Algebras su(N): An Introduction* (Birkhäuser Basel, 2003).

[57] P. Weinberg and M. Bukov, "QuSpin: a Python package for dynamics and exact diagonalisation of quantum many body systems. part II: bosons, fermions and higher spins", SciPost Phys. **7**, 020 (2019).

[58] L. Pitaevskii and S. Stringari, *Bose-Einstein Condensation and Superfluidity* (Oxford University Press, 2016).

[59] C. J. Pethick and H. Smith, *Bose-Einstein Condensation in Dilute Gases*, 2nd ed. (Cambridge University Press, 2008).

[60] W. M. C. Foulkes, L. Mitas, R. J. Needs, and G. Rajagopal, "Quantum Monte Carlo simulations of solids", Rev. Mod. Phys. **73**, 33–83 (2001).

[61] A. Minguzzi, S. Succi, F. Toschi, M. P. Tosi, and P. Vignolo, "Numerical methods for atomic quantum gases with applications to Bose-Einstein condensates and to ultracold fermions", Phys. Rep. **395**, 223–355 (2004).